The H1 Trigger for Neutral Current Deep Inelastic Scattering Events at Low Q^2

Dissertation

zur Erlangung des Doktorgrades
des Fachbereichs Physik
der Universität Hamburg

vorgelegt von
Tibor Kurča
aus Košice

Hamburg
1993

Gutachter der Dissertation:	Prof. Dr. H.-H. Duhm Prof. Dr. W. Bartel
Gutachter der Disputation:	Prof. Dr. H.-H. Duhm Prof. Dr. E. Lohrmann
Datum der Disputation:	17.12.1993
Sprecher des Fachbereichs Physik und Vorsitzender des Promotionsausschusses:	Prof. Dr. E. Lohrmann

Abstract

The experiments at the e^-p storage ring HERA have opened entirely new kinematical domains for the measurement of the proton structure functions. Interesting physics results are expected at high momentum transfers $Q^2 \rightarrow 10^5\ GeV^2$, but also in very low x, Q^2 region. The topic of this thesis is the study of the design of a dedicated electron trigger (BSET) for the backward electromagnetic calorimeter (BEMC) at H1. A further task is the elaboration of efficient trigger algorithms for neutral current deep inelastic scattering (NC DIS) at low Q^2 ($Q^2 < 100\ GeV$), using the available triggers of the H1 detector. Physics rates for NC DIS at $Q^2 < 100\ GeV^2$ are relatively high ($\sim 1\ Hz$), but on the other hand the total background rate at a full design luminosity is expected to be much larger ($\sim 100\ kHz$). The main goal is to reduce the L1 trigger rate down to $\leq 100\ Hz$ and simultaneously to keep a high trigger efficiency for NC DIS events in the whole kinematical region of interest. The designed trigger has been realized and has worked successfully from the very beginning of the data taking at HERA. Different methods to check the technical performance of the trigger on-line as well as off-line and to calculate the trigger efficiency for NC events are developed. Analysis of the data triggered by the BSET in 1992 is made, and on the top of the standard selection criteria additional ones, using detailed trigger and data acquisition information, are applied.

Zusammenfassung

Die Experimente am e^-p HERA Speicherring haben vollständig neue kinematische Gebiete für die Messung der Strukturfunktionen des Protons eröffnet. Interessante physikalische Ergebnisse werden sowohl bei hohen Impulsüberträgen $Q^2 \rightarrow 10^5\ GeV^2$ als auch bei sehr kleinen Werten der kinematischen Variablen x, Q^2 erwartet. In der vorliegenden Arbeit werden Studien zum Design eines Elektron-Triggers (BSET) für das elektromagnetische Rückwärtskalorimeter (BEMC) des H1-Detektors dargestellt. Weitere Untersuchungen betreffen die Erstellung von effizienten Trigger-Algorithmen für die tiefinelastische Streuung bei neutralen Strömen (NC DIS) und kleinen Q^2 ($Q^2 < 100\ GeV$) unter Berücksichtigung aller verfügbarer Subtrigger des H1-Detektors. Die Raten für NC DIS Ereignisse mit $Q^2 < 100\ GeV^2$ liegen relativ hoch ($\sim 1\ Hz$), aber es wird erwartet, daß die totale Rate von Untergrundereignissen bei der Design-Luminosität Werte bis $\sim 100\ kHz$ erreichen kann. Die wesentliche Aufgabe ist die L1-Triggerrate auf einen Wert $\leq 100\ Hz$ zu bringen und gleichzeitig eine hohe Trigger-Effizienz für den kinematisch interessanten Bereich zu garantieren. Der entworfene Trigger wurde realisiert und erfolgreich seit Beginn der Datennahme bei H1 eingesetzt. Verschiedene Methoden zur Funktionskontrolle des Triggers während und nach der Datennahme (On- und Offline), sowie zur Berechnung der Trigger-Effizienz physikalischer NC Ereignisse wurden entwickelt. Die Datenanalyse der durch den BSET getriggerten NC DIS Ereignisse wurde zuerst mit den Standard-Selektionskriterien durchgeführt und später um zusätzliche Selektionskriterien unter Berücksichtigung detailierter Trigger- und Dateninformationen erweitert.

*" Dedicated to the memory of
my father Karol Kurča"*

Contents

Introduction

> *" ... even with the best evidence available at any one time, no one can predict how any one class of experiment or any theory may turn out, and which will be the best way ahead..."* D.H. Perkins, Workshop Experimentation at HERA, Amsterdam 1983

First serious considerations on building an electron-proton collider in Europe date back to the beginning of the seventies [1]. In the following years intensive studies on the possibility to build such a machine at CERN and DESY were done under the auspicies of ECFA [1]. Two important decisions of the European High Energy Physics community opened the way for DESY as a site for the future electron-proton collider: the decision to build a $p\overline{p}$ collider and as a long-term program an e^-e^+ collider LEP, both at CERN. When taking into account other facillities, existing or under construction (Tevatron, Isabelle), the need to complement this program of high energy physics research raised the interest in an e^-p machine. In October 1979 the DESY Scientific Policy Committee decided to present to the German authorities the proposal for HERA (Hadron-Elektron-Ring-Anlage) and in February 1981 the unique scientific value of this project was recognized by the German Federal Government Comittee and principal recommendation to construct the e^-p collider was given.

The pointlike nature of leptons makes them particulary well-suited probes of the more complicated nucleon structure. Not surprisingly, especially processes with a large Q^2 momentum transfer, which due to the uncertainity principle probe very short distances, were in the center of interest [2],[3].

Concentration on the high $Q^2 > 100\ GeV^2$ physics has found its reflection also in the H1 detector and trigger design [2],[3],[4]. For the backward region, i.e. for the scattered electron angle $\theta_e > 145°$ (see Fig. 2.3), only very raw hadronic energy measurement was foreseen and even for the electron measurement the angular coverage down to only 170° was considered sufficient and the task of the trigger was defined this way [2]:

> "The aim of the trigger is to collect all interesting physics events with minimal background. In reality this means all events with $Q^2 \geq 100\ GeV^2$ together with a sample of lower Q^2 events..."

This attitude has its roots of course in the general status of the knowledge at that time. E.g. the limit on the top quark mass was at $\geq 40\ GeV$ and this was still within the HERA reach. On the other hand the precision of the QCD calculations was e.g. insufficient to estimate the higher twist contribution. Thus it was hard in the region of low Q^2 to distinguish if the scaling violations in the structure functions measurements vary logarithmically or according to a power law as predicted by other strong interaction theory candidates. Scattering experiments with large momentum transfers $Q^2 > 100\ GeV^2$ are

[1] European Committee for Future Accelerators

free from potential nonperturbative, mass and higher twist effects. Additionaly one can hope that at some sufficiently large Q^2 the quark substructure could be revealed.

Later, with the progress in the theory as well as in the experiment, the importance and interest for low $Q^2 < 100\ GeV^2$ physics has grown. The HERA workshop 1987 already realized the importance and potential of the very low x, low Q^2 region. Theoretical considerations suggested that at very low x the structure functions may in fact behave drastically differently from any of the available extrapolations [5]. But still the detailed studies were devoted mostly to structure functions measurement at $Q^2 > 100\ GeV^2$.

In the late 1989 the urgent need for an inclusive electron trigger in the backward H1 region was realized. The detailed background studies showed that with the originally proposed trigger on the total energy of the Backward ElectroMagnetic Calorimeter (BEMC), the access to the low (x, Q^2) physics at high y would be very limited. Consequently it was decided to build a dedicated single electron trigger based on the design of the BEMC, which was already being constructed.

The task of this thesis is the detailed design simulation of the Single Electron Trigger (BSET) for the BEMC and preparation of the trigger algorithms for the NC DIS at $Q^2 < 100\ GeV^2$. After successful realization of the BSET trigger, its performance during the data taking period in 1992 was checked and the trigger efficiencies for the physics analysis were determined.

The thesis is structured into the following Chapters:

In the **Chapter 1** the basics of the DIS physics, kinematics and experimental measurement of the variables of interest are presented.

In the **Chapters 2** and **3** the main components of the H1 detector and the trigger are described. Emphasis is put on the trigger elements used later for the simulation of the trigger algorithms for NC DIS events. Specifications of triggering at HERA 96 ns bunch crossing intervals are described and the importance of pipelining and multilevel trigger scheme is discussed.

Chapter 4 is devoted to the general aspects of triggering on NC DIS events. The basic requirements on the triggers and main background sources are given.

In the **Chapter 5** the BSET trigger design simulations results are presented. From the studies of the behaviour of electromagnetic and hadronic showers in the BEMC basic trigger elements are defined. The BSET trigger detects well localized energy deposits, corresponding to the electromagnetic clusters. Subtriggers, i.e. combinations with trigger elements available from other subdetectors, and trigger algorithms for triggering on the low (x, Q^2) NC DIS processes are proposed. These algorithms are optimized in order to suppress the unwanted background events to the acceptable rate ($\leq 100\ Hz$).

Hardware realization of the BSET trigger is described in the **Chapter 6**.

In the **Chapter 7** the BSET trigger performance in the real data taking is analysed. Correlations between trigger energies and off-line reconstructed quantities are shown. Tools to check the technical performance by on-line monitoring, using the monitor triggers and logic consistency checks are developed. The trigger thresholds calibration is provided and the physics trigger efficiency for the low (x, Q^2) NC DIS is calculated. Pileup studies and studies of an unexpected source of background events are done.

In the **Chapter 8** the physics analysis of the measured data in the new kinematical domain with two additional selection criteria is performed.

At the end, in the **Summary**, the main results of all chapters are briefly summarized.

Finally in the **Appendices A** and **B** a short description of the H1 software environment resp. basic BEMC material constants and parameters important for the showers development is given.

Chapter 1

Physics at HERA

1.1 Deep Inelastic Scattering

Deep inelastic lepton-nucleon scattering (DIS) has played a dominant role in the study of the basic structure of the matter and contributed significantly to the understanding of the electromagnetic, weak and strong interactions at the quark-parton level.

To penetrate deeper into the matter, to probe the nucleon structure with much better resolution [1], the large electron-proton collider HERA (Hadron-Elektron-Ring- Anlage) has been completed at DESY Hamburg in the year 1991. All previous DIS measurements were performed at fixed target experiments but at HERA for the first time two DIS experiments with assymetric colliding beams were built. In the late spring 1992 the first physics collisions in both detectors H1 and ZEUS were observed.

Electrons and protons colliding at nominal energies $E_e = 30\,GeV$ resp. $E_p = 820\,GeV$ will provide a centre of mass energy of 314 GeV. This is equivalent to a 50 TeV electron beam hitting a hydrogen fixed target. This opens up an entirely new kinematical region for DIS physics.

In the first years HERA was operated at a slightly smaller electron beam energy of $E_e = 26.7 GeV$, providing an energy of 296 GeV in the centre of mass system.

With the design luminosity of $1.5 \cdot 10^{31} cm^{-2} s^{-1}$ the proton structure will be explored in a domain which is two orders of magnitude smaller in x-Björken and two orders of magnitude larger in the square of 4-momentum transfer Q^2, than what has been reached in fixed target experiments (Fig. 1.3). Measurements at values down to $x \sim 10^{-4}$ at small Q^2 and at $Q^2 \geq 10^4$ at higher x values will be possible.

New, precise measurements of the nucleon structure functions at low and very low x are an important input for theoretical predictions of cross sections at future colliders such as the LHC and the SSC.

Due to the fact that Q^2 values $\geq M_Z^2$ are achievable, electroweak parameter measurements at HERA can be done. At these Q^2 values the weak process contributions to the cross sections are of the similar size as those due to the electromagnetic processes. Simultaneous measurement of the neutral and charged current interactions (NC resp. CC) gives the HERA machine the potential of the former lepton and neutrino DIS experiments.

The gap between the kinematical regions accessed by the fixed target and HERA experiments at the design energy (Fig. 1.3) will be covered by HERA operation at lower beam energies. The minimal e^- beam energy is determined by the injection energy into the HERA machine (12 GeV) and minimal proton beam energy is limited by the requirement of keeping reasonable luminosity (300 GeV).

[1] $Q^2 \sim 10^5\, GeV^2$ corresponds to spatial resolution of about $10^{-18} m$.

The fact that HERA is foreseen to provide also longitudinally polarised electron or positron beams extends the physics potential of this machine. Experiments with polarised internal gas targets will enable to get more information about the spin distributions in the protons and the neutrons.

1.2 Kinematics

Inclusive DIS of leptons on nucleons $e^-p \to lX$ (Fig. 1.1) provides the most direct way to measure the nucleon structure functions F_1 and F_2. These structure functions are directly related to the differential cross section of this scattering process (1.24). Thus inevitable prerequisite to study the nucleon structure is a sufficiently precise measurement of the differential cross-sections for the charged - $e^-p \to \nu_e X$, and/or neutral current - $e^-p \to e^-X$ scattering processes. NC cross-section involves γ and Z^0 exchange as well as the interference between the two. In the case of CC interaction in our experiment the exchanged particles are W^- bosons. The rates of NC and CC interactions are comparable only at $Q^2 > 5000\ GeV^2$, below $Q < 100\ GeV^2$ the rate of NC events is by two orders of magnitude higher than those of CC [8]. In our studies we will concentrate only on the NC DIS processes.

The cross-section of the $e^-p \to e^-X$ process depends on two independent variables, besides the energy s. In the experiment the polar angle θ_l (θ_j) and the corresponding energy $E_l(E_j)$ of the scattered lepton (current jet) are measured. From these two quantities all other global variables can be calculated. From the scattered quark originates the current jet. Non-interacting proton constituents (spectators) emerge in the final state as a proton or target jet (remnant jet). At HERA we take the convention that the direction along the incoming proton is the forward direction with $+z$ coordinate and $\theta = 0°$. The backward hemisphere is defined by the the incoming electron direction and $\theta \to 180°$.

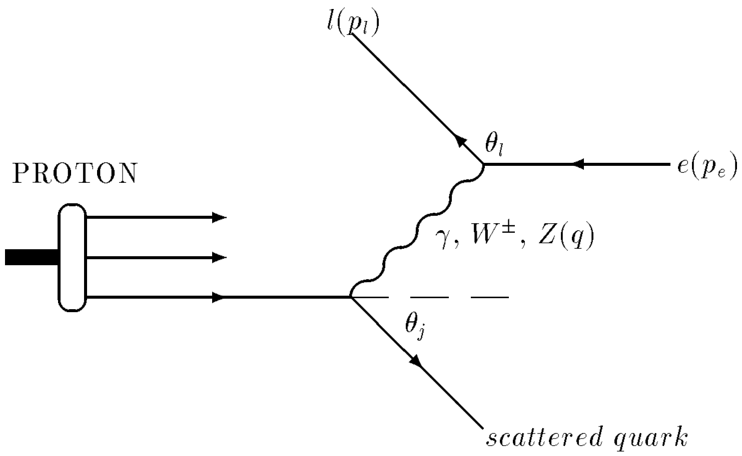

Figure 1.1: Basic diagram for deep inelastic scattering in the quark-parton model.

However, the DIS cross sections and structure functions are usually expressed in terms of Q^2 and x because of the simple interpretation of these variables in the quark-parton model.

Denote p_e, p_l, P the 4-momenta of the incoming and scattered lepton and the incoming proton, respectively, and E_l, θ_l the energy and angle of the scattered lepton. When neglecting the masses of the electron, proton and the scattered lepton we obtain the following relations between the kinematic variables characterizing DIS:

$$s = (p_e + P)^2 \approx 4E_eE_p \tag{1.1}$$

$$Q^2 = -q^2 = -(p_e - p_l)^2 \tag{1.2}$$

$$x = \frac{Q^2}{2P \cdot q} \tag{1.3}$$

$$y = \frac{P \cdot q}{P \cdot p_e} = \frac{2P \cdot q}{s} \tag{1.4}$$

$$W^2 = (q + P)^2 \approx \frac{1 - x}{x} Q^2 \tag{1.5}$$

Since there are only two degrees of freedom, any two of the above mentioned variables can be used as independent variables for cross section formulae, but (x, y) and (x, Q^2) are most commonly used. For more details on the kinematical variables see [6].
The physical interpretation of these variables is the following:

- $\boldsymbol{s}$ - square of the energy in the centre of mass system
- $\boldsymbol{Q^2}$ - square of the 4-momentum transfer, defines the resolution by which the electron probes the short distance structure of the nucleon
- $\boldsymbol{x}$ - Björken scaling variable (in naive QPM momentum fraction of the nucleon carried by the struck quark)
- $\boldsymbol{y}$ - scaling variable, describing energy transfer from the incoming to the outgoing lepton in the rest frame of the proton
- $\boldsymbol{W}$ - total mass of the hadronic final state

1.3 Topological characteristics of NC DIS events

Due to the large difference between the electron and proton beam energies the shape of the phase space for the scattered lepton and quark is very elongated and very assymetric events in the laboratory system will be produced. Most of the final state hadrons will be distributed in the forward direction, i.e. along the incoming proton.

Mainly the losses in the very forward direction (beam pipe effect) are responsible for the missing overlap between the HERA (x, Q^2) measurable domain and that of fixed targets experiments' domain [7].

The Jacquet-Blondel method [9] (J-B method) extends the measurable domain at HERA at high $Q^2 \geq 100$ and at $x \geq 0.01$, but there still remains a gap which could be overlapped only by HERA running at smaller beam energies than the design ones.

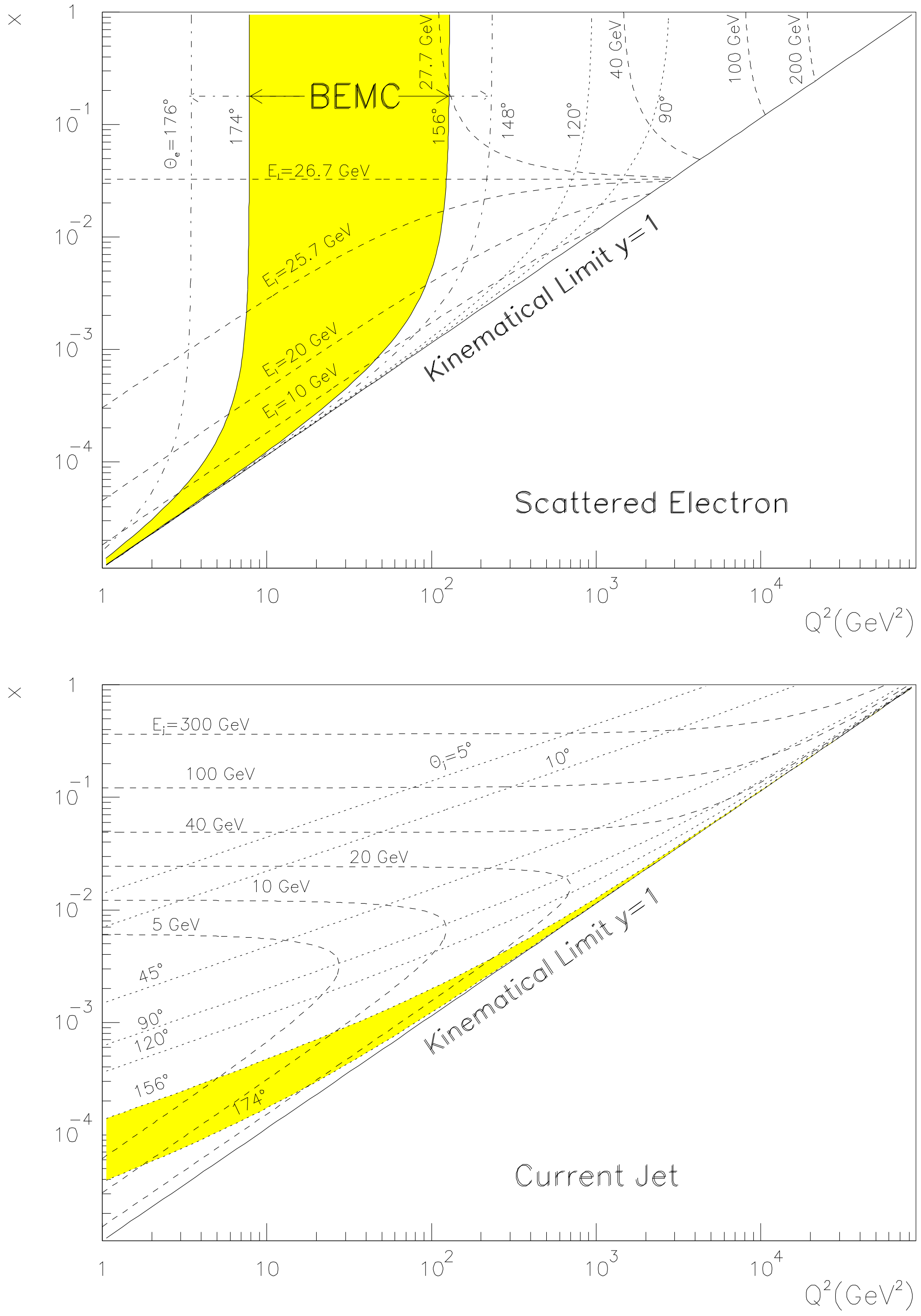

Figure 1.2: *Scattering angle and secondary energy of electron and current jet. The angular acceptance of the BEMC is shown for both.*

Kinematical equations can be illustrated in the (x, Q^2) plane by the isolines of constant electron θ_e and hadronic current jet θ_j scattering angles or by lines of constant electron and current jet energies E_e, resp. E_j (Fig. 1.2).

At high Q^2 values electrons are scattered mainly into the central detector part and current jets are found in the central or forward detector part. In this kinematical region, from the trigger point of view, we rely on the liquid argon (LAr) electron trigger and eventually on a trigger based on the topological energy sums such as barrel or transversal energy.

For this kind of events also the tracker triggers will be very useful and this redundancy will be used for cross checking of the performance of the triggers.

Below $Q^2 \approx 100\ GeV^2$ the electron will be scattered into the backward hemisphere, into the angular acceptance of the backward electromagnetic calorimeter (BEMC). The BEMC is integrated into the LAr trigger scheme, but it has also its own electron trigger (BSET) [53]. This trigger was designed with the aim to make a better use of the BEMC granularity, allowing efficient suppression of the high background rate. Electrons at very low Q^2 ($Q^2 \leq 5 - 10\ GeV^2$) are escaping in the beam pipe due to the BEMC angular acceptance limit $\approx 175°$. A fraction of these events can be detected due to the smearing of the interaction vertex in z coordinate, i.e. along beams direction (see page 21). The region of low Q^2 and very low x, i.e. where struck quarks are almost at rest since they carry only a tiny part of the proton momentum, can be considered as the fixed target HERA domain [7].

The characteristics of events at low x - high y values is that the hadron jet and scattered electron go both backwards under big scattering angles and with small electron energy. The smaller the electron energy, the bigger the energy of the hadronic jet accompanying the electron. This kinematic domain is the most difficult one for efficient NC DIS trigger due to the high rates of the beam-wall and photoproduction background events. Another very interesting feature of the HERA kinematics is the existence of the so called kinematic peak (see Fig. 8.2). From the relation between electron energies before and after scattering (1.2) and y as the measure of electron energy losses (1.3) one can find in the region of small y a wide range of practically constant electron energy $E_e \simeq E_l$ (Fig. 1.2). This property enables precise energy calibration of the BEMC from the measured data.

1.4 Reconstruction of the kinematical variables

1.4.1 Introduction

Previous DIS experiments relied on the measurement of the scattered lepton to measure the internal structure of the nucleon.

HERA interactions resemble more a collision in the center of mass rather than a classical e^-p scattering, and more extensive use of hadronic flow measurement can be used than in the fixed target measurements. Three domains in the (x, Q^2) plane (Fig. 1.3) can be identified where the measurement is possible [10]:

- only electron measurement
- only hadrons measurement

- combined electron and hadrons measurement

The precision with which the kinematical variables can be reconstructed directly influences the measured differential cross sections. In different regions of the (x, Q^2) plane various systematic uncertainties affect the measurement. Main sources of the systematic errors are:

- absolute calibration of the energy measurement
- energy resolution
- detector alignment - scattering angle measurement

Measurement errors on the (x, Q^2) initiate so-called migration effects. The measured event rate in a given (x, Q^2) bin is not the true one. In fact it is a mixture of events migrating from the adjacent bins into this bin and the fraction of events remaining in this proper bin. The product of both migrations $A(x, Q^2)$ is called *smeared acceptance*. The observed and true cross sections are then simply related by:

$$\sigma_{true}(x, Q^2) = \frac{\sigma_{obs}}{A(x, Q^2)} \tag{1.6}$$

The smeared acceptance depends on the detector resolution and also on the relative events rates in the bins.

1.4.2 Electron measurement only

This method of x and Q^2 reconstruction from the energy and angle of the final state electron is the conventional one used in previous fixed target experiments. The most stringent limit to a precise measurement of structure functions is coming from the absolute energy calibration. The absolute energy scale must be known at the $1-2\%$ level. A systematic calibration error of 1% generates a systematic shift of the differential cross section which rises inversely proportional to y, reaching already 10% at $y \sim 0.1$ value [10]. The basic kinematical variables can be expressed in terms of the scattered electron energy E_l and angle θ_l in the laboratory frame:

$$Q^2 = 4E_eE_lcos^2\frac{\theta_l}{2} \tag{1.7}$$

$$x = \frac{E_eE_lcos^2(\theta_l/2)}{E_p(E_e - E_lsin^2(\theta_l/2)} \tag{1.8}$$

$$y = \frac{E_e - E_lsin^2(\theta_l/2)}{E_e} \tag{1.9}$$

From kinematical equations (1.7-1.9) we obtain the following relations for measured uncertainities:

$$\frac{\delta Q^2}{Q^2} = \frac{\delta E_l}{E_l} - tan\frac{\theta_l}{2}\delta\theta \tag{1.10}$$

$$\frac{\delta x}{x} = \frac{1}{y}\frac{\delta E_l}{E_l} + tan\frac{\theta_l}{2}(x\frac{E_p}{E_e} - 1)\delta\theta \tag{1.11}$$

$$\frac{\delta y}{y} = \frac{y-1}{y}\frac{\delta E_l}{E_l} + \frac{1-y}{y}cot\frac{\theta_l}{2}\delta\theta \tag{1.12}$$

The kinematical reconstruction from the electron variables is independent of any assumptions about the hadronic final state and for the x, Q^2 measurement following consequences can be drawn [10]:

- The resolution in x at low y due to the factor $1/y$ is very bad. Measurement of x at y below 0.1 is hardly achievable with sampling calorimeters
- It is important that this strong y dependence is independent from the incoming energies. It is therefore possible to extend, at given x and y, the region of precise measurement of x down to lower Q^2 by running HERA at lower beam energies.
- The error on x due to the precision of the angle measurement is significant only at large x and low Q^2
- At large y the electroweak radiative corrections to be applied are large (up to 100% of the Born cross section) and are the major limitation on the measurable highest Q^2 at a given x.
- The Q^2 measurement is very good with the possible exception at large angles ($\theta \geq 170^o$), and only if the angular resolution is worse than a few $mrad$ [11].

1.4.3 Hadronic flow measurement only

Some limitations of the electron measurement can be overcome by kinematics reconstruction from the hadronic final state. A method to determine x and Q^2, proposed by A. Blondel and P. Jacquet [9], is based on two assumptions:

- x and Q^2 measurement from only outgoing hadronic flow is possible without using any jet identification algorithm or proton structure hypothesis
- for HERA kinematics, it is more suitable to express y and Q^2 in terms of laboratory variables using the energy-momentum balance between lepton and hadronic system and then to deduce x

Replacing the momentum transfer q in equation (1.4) by $(p_h - P)$, where p_h is the 4-momentum of the total outgoing hadronic system, gives:

$$y = \frac{P \cdot (p_h - P)}{P \cdot p_e} \tag{1.13}$$

with

$$p_h = \sum_h (E_h, p_{xh}, p_{yh}, p_{zh})$$

we obtain

$$y_{jb} = \sum_h \frac{E_h - p_{zh}}{2E_e} \tag{1.14}$$

Combining equations (1.7) and (1.9) we get on the lepton side:

$$Q^2 = \frac{(E_l sin\theta_l)^2}{1 - y} \tag{1.15}$$

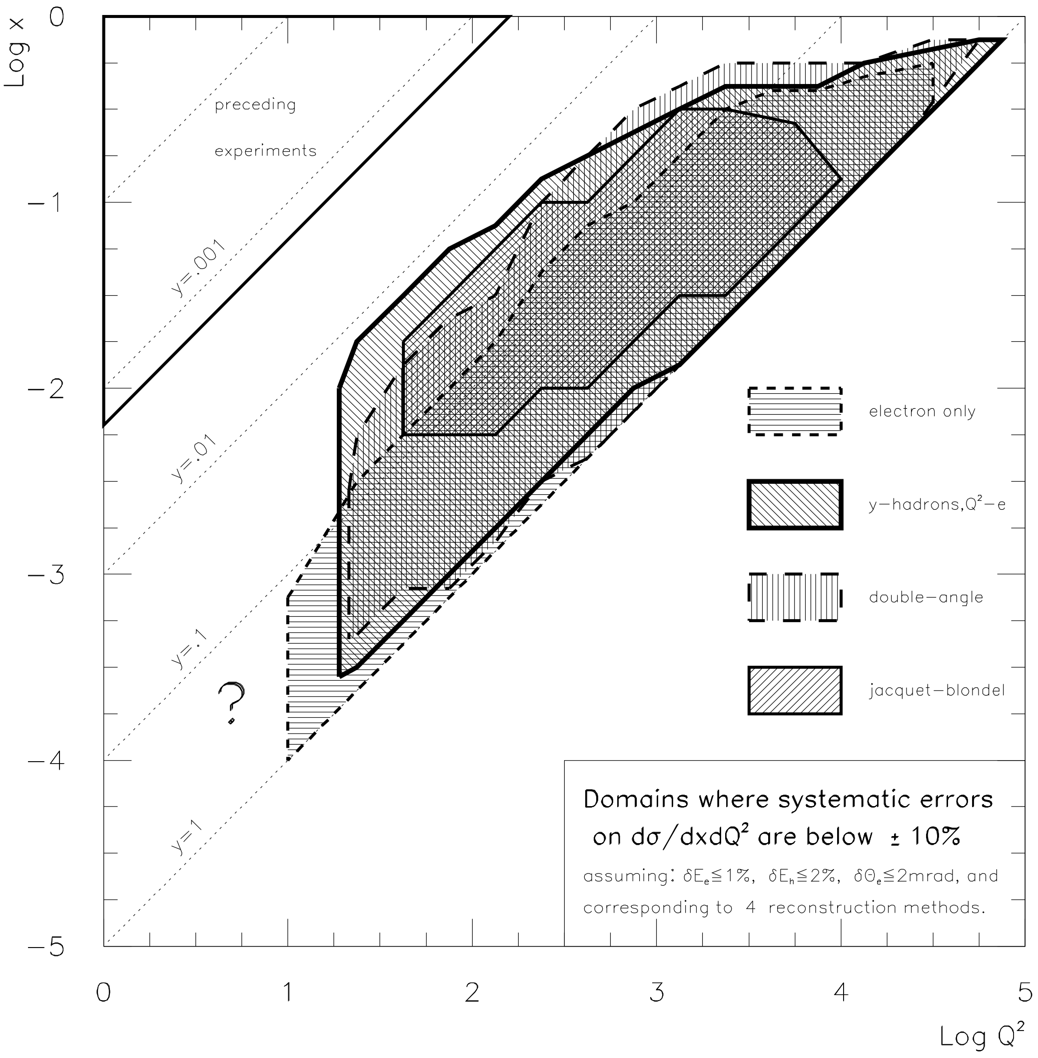

Figure 1.3: *Kinematical regions (for electron beam $E_e = 30$ GeV) where different reconstruction methods can be used [11]. In the left upper corner the region studied by previous fixed target experiments is shown.*

which on the hadronic side leads to:

$$Q^2_{jb} = \frac{p_t^2}{1-y} = \frac{(\sum \vec{p_{th}})^2}{1-y} \tag{1.16}$$

where p_t is the total transverse momentum of the hadron flow and $\vec{p_{th}}$ is the transverse momentum of the hadron h.

It can be seen from equations (1.14) and (1.16), that the variables y and Q^2 defined by J-B method are very well tailored for the HERA detectors, because the hadrons emitted into the very forward region (with the unavoidable beam pipe cut) contribute only very little to the measured y, Q^2.

1.4.4 Combined methods from electron and hadrons measurements

From the measured energies and angles of the final state electron (E_l, θ_l) and current jet from the struck quark (E_j, γ_j) one can combine another methods of the x, Q^2, y reconstruction. All methods are influenced differently by the detector effects. It turns out that only the so-called double angle method (measurement of θ_l, γ_j) and measurement of Q^2 from E_l resp. y_{jb} by J-B method can provide the required precision [12].

When using the double angle method the reconstructed kinematical quantities are calculated from the following relations:

$$y_{\theta,\gamma} = \frac{sin\theta(1-cos\gamma)}{sin\gamma + sin\theta - sin(\gamma+\theta)} \tag{1.17}$$

$$Q^2_{\theta,\gamma} = 4E_e^2 \frac{sin\gamma(1+cos\theta)}{sin\gamma + sin\theta - sin(\theta+\gamma)} \tag{1.18}$$

$$x_{\theta,\gamma} = \frac{E_e}{E_p} \frac{sin\gamma + sin\theta + sin(\theta+\gamma)}{sin\gamma + sin\theta - sin(\theta+\gamma)} \tag{1.19}$$

The above mentioned method of *mixed* variables, i.e. Q^2 is taken from electron measurement and y from the J-B method, leads to the using of the relations:

$$y_{mix} = y_{jb} \tag{1.20}$$

$$Q^2_{mix} = Q^2_{el} \tag{1.21}$$

$$x_{mix} = \frac{Q^2_{el}}{s y_{jb}} \tag{1.22}$$

The *mixed* method gives acceptable x, Q^2 measurement in the region $y \geq 0.01$ Fig. 1.3 [11].

1.5 Nucleon Structure Functions

1.5.1 Introduction

The first measurements of the the structure functions F_1 and F_2 made at the end of the 60's at SLAC marked the beginning of a modern era of nucleon structure investigations. Mainly two results of the experiments with high energy electron beams ($E_e \rightarrow 20\ GeV$) scattered off the nuclear targets indicated that a new structural level has been achieved:

- the measured cross section for scattering at large angles exceeded the expected one by more than one order of magnitude
- both structure functions F_1 and F_2 appeared to depend mainly on x; moreover they tended to a finite value even when both Q^2 and ν were large, as long as the ratio Q^2/ν was kept constant ($x = \frac{Q^2}{2m_p\nu}$)

The second result known as scaling of the nucleon structure functions, predicted by J.D. Björken [13], strongly contrasted with the properties of elastic form factors, which rapidly vanish with increasing Q^2 [14]. The new phenomena were explained as an evidence for the pointlike structure of the nucleons (see [15]). The virtual photon, as a probe, can be scattered by the collection of quasifree pointlike, electricaly charged objects - Feynman partons, later identified with the quarks (quark parton model - QPM).

In this picture the DIS cross-section is regarded as the incoherent sum of individual photon-parton cross-sections. In the high proton momentum limit ($P \to \infty$) the Björken x variable is just the fraction of the proton's momentum carried by the elastically scattered parton. The size of this cross-section is then proportional to the probability $q_f(x)$ of finding a quark of flavour f and the momentum xp in the proton.

Further experiments revealed some apparent inconsistencies in the simple QPM picture of the DIS. In 1972 it became clear that quarks carried only ~ 0.5 of the proton's momentum [16] and in 1975 significant scaling violations were observed at SLAC and FERMILAB [17]. The explanation was provided by a non-abelian gauge theory of strong interactions: quantum chromodynamics (QCD). According to the QCD the nucleon contains not only charged partons (quarks) but also electrically neutral, massless, spin 1 objects, called gluons. Quarks in the nucleon interact with each other by exchanging the gluons which are the carriers of the strong force. For the structure functions it means that they are no longer dependent on x only but on both x and Q^2. The missing momentum fraction of the nucleon was also cured, it was attributed to the gluons.

In analogy with QED, quarks may radiate gluons ($q \to qg$) and gluons may convert into $q\overline{q}$ pairs ($g \to q\overline{q}$). Unlike the electrically neutral QED photons, gluons, carrying colour charge, may couple directly to each other. Therefore in the QCD there exist additional diagrams of the $g \to gg$ and $gg \to gg$ type corresponding to the gluon selfcoupling. The interactions between quarks and gluons are governed by the QCD coupling constant which in the first loop approximation has the following form:

$$\alpha_s(Q^2) = \frac{12\pi}{(33 - 2N_f)\ln(Q^2/\Lambda^2)} \tag{1.23}$$

where N_f is the number of quark flavours and Λ is a mass scale parameter, the only free parameter in the theory to be determined from an experiment. As it is seen from (1.23) the QCD posses the so-called asymptotic freedom property, i.e. when $Q^2 \to \infty$ then $\alpha_s \to 0$, enabling perturbative calculations at sufficiently large Q^2. This way the QPM treatment of essentially free quarks is contained also in the QCD theory. The QPM became very successful in describing all processes with large momentum transfers (hard processes) from leptons to hadrons, or even from hadrons to hadrons and is considered as the Born approximation of the perturbative QCD theory. Non-perturbative approaches are these days still in their infancy. They face big technical, computational problems and yet do not have a strong predictive power.

The series of further DIS experiments at CERN (EMC, BCDMS) and FERMILAB, using beams of high energy muons and neutrinos, extended the SLAC measurements of the structure functions to the significantly higher values of Q^2 ($\rightarrow$ 200 GeV^2) and lower x values (>0.01). The HERA experiments are now pushing these limits of Q^2 beyond 10^4 GeV^2 and of x down to 10^{-4}. This is a big leap towards the frontiers where the signs of a new physics are expected.

1.5.2 Structure Functions and Parton Distributions

The differential cross section for unpolarized $e^-p \rightarrow e^-X$ scattering in lowest order of the electroweak coupling constant α can be written in terms of three structure functions $F_1(x,Q^2)$, $F_2(x,Q^2)$ and $F_3(x,Q^2)$:

$$\frac{d^2\sigma}{dxdQ^2} = \frac{4\pi\alpha^2}{xQ^4}[xy^2F_1(x,Q^2) + (1-y)F_2(x,Q^2) + (y - \frac{y^2}{2})xF_3(x,Q^2)] \tag{1.24}$$

For $Q^2 < 500\,GeV^2$ the contribution to the cross section from the exchange of the Z^0 boson is negligible and the xF_3 structure function can be neglected [7]. The DIS cross section in the kinematical region considered is determined by the two structure functions F_1 and F_2, which are related via $2xF_1 = F_2/(1+R)$:

$$\frac{d^2\sigma}{dxdQ^2} = \frac{2\pi\alpha^2}{xQ^4}[2(1-y) + \frac{y^2}{1+R}]F_2(x,Q^2) \tag{1.25}$$

Unlike real photons, the exchanged virtual photon can have a longitudinal as well as the transverse polarization. By R we denote the ratio of the corresponding cross sections σ_L and σ_T for the absorption of longitudinaly and transversely polarized virtual photons.

F_1 and F_2 can be unambiguously separated only from the measurements at different beam energies. If only a measurement at one energy is available, an assumption about the value of R has to be made.

The measured structure function F_2 is in the QPM interpreted as a linear combination of the quark $q_f(x,Q^2)$ and antiquark $\overline{q}_f(x,Q^2)$ momentum distribution functions:

$$F_2(x,Q^2) = \sum_f A_f(Q^2)[xq_f(x,Q^2) + x\overline{q}_f(x,Q^2)] \tag{1.26}$$

The flavour-dependent coefficient A_f involves at low Q^2 only the quark electric charge e_f^2 and F_2 reduces to the electromagnetic structure function F_2^{em}.

Specific quark distribution functions can be isolated from the so-called global fits [18], i.e. by combining the information from DIS experiments with different beams (e^-, μ, ν, $\overline{\nu}$). The procedure starts with parametrization of q_f at a sufficiently large $Q_0^2 \sim 4-5\ GeV^2$. Then the $q_f(x,Q^2)$ can be calculated at higher Q^2 from next-to-leading order (NLO) perturbative QCD. For example the MRS parametrization [18] of the parton distributions (valence, sea quark and gluon) at $Q^2 = Q_0^2$ is of the form:

$$xu_v = N_1x^{\eta_1}(1-x)^{\eta_2}(1+\eta_3x) \tag{1.27}$$

$$xd_v = N_2x^{\eta_4}(1-x)^{\eta_5}(1+\eta_6x) \tag{1.28}$$

$$2x(\overline{u}+\overline{d}+\overline{s}) = A_s x^{-\lambda}(1-x)^{\eta_s} \tag{1.29}$$

$$xg = A_g x^{-\lambda}(1-x)^{\eta_g} \tag{1.30}$$

where $u_v = u - \overline{u}$ etc. There are thus more than 10 parameters $(\eta_i, A_s, (A_g), \lambda_{QCD})$ to be determined by the data for $Q^2 > Q_0^2$. The coefficients N_1 and N_2 are fixed by the flavour sum rules, and A_g (or A_s) by the momentum sum rule. Usually it is assumed that the sea quarks distributions satisfy the $\overline{u} = \overline{d} = 2\overline{s}$ condition. Recent NMC data [19], violating the Gottfried sum rule, initiated big discussions on the precise u and d content of the sea. The contribution of heavy sea quarks (c and b) is usually included via gluon annihilation process $g \to Q\overline{Q}$.

Gluon distribution is a dominating component in the low x DIS. It has been difficult to measure its properties due to the absence of direct coupling between the gluon and the electroweak bosons. At low x we enter the region where non-perturbative effects starts to play a non negligible role and therefore measurements at HERA are supposed to be a challenge for theoretical physicists to solve the QCD in the non-perturbative regime. Naive QPM and Regge theory (with $\alpha_P = 1$) imply that $\lambda = 0$. However there are good theoretical reasons why λ may be as large as 0.5, as will be discussed in the next section.

1.5.3 Structure Functions at Low x

The x and Q^2 dependence of parton distributions at very small x, where the dynamics of DIS becomes dominated by the gluons, is one of the most promising domains in QCD [10]. A large amount of different sets of structure function parametrisations exist today (see e.g. [20]) describing rather well the available experimental data. But extrapolation to low x gives rise to huge discrepancies among the different parametrisations. The theoretical interpretation is not unambigous today and first data already brought constraints, which allow to exclude some of the most diverging predictions [36].

In the domain of standard DIS ($Q^2 \to \infty$ at fixed x) we have a rather good (complete) understanding of QCD dynamics. Standard QCD evolution equations of Gribov, Lipatov, Altarelli and Parisi (GLAP) [21] are based upon solid tools of field theory. Splitting functions,considered as the central elements of this approach, describe a cascade of quarks and gluons decays. In this process partons loose longitudinal momentum but gain transversal one (virtuality). In the region of small x and Q^2 the evolution gets dominated by gluons alone and the gluon splitting functions should be replaced by the so-called Fadin-Kuraev-Lipatov kernel (FKL) [22] which describes more precisely the main contribution $\alpha_s \ln 1/x \cdot \phi(q^2)$ with the exact function $\phi(q^2)$ (not only the approximate term $\phi(q^2) \sim \ln q^2$ which leads to the $\ln q^2$ dependence as in the GLAP case). Numerical studies [23] indicate that for the gluon distribution the differences between GLAP and FKL are small at HERA energies. Characteristic behaviour of parton distributions at low x in the perturbative QCD results from the summation of soft gluon emissions via the GLAP or FKL equations. It gives at small $x \ll 1$, $\lambda = 12\alpha_s \ln 2/\pi$ at fixed coupling α_s. So the expected gluon and sea quark distributions behave as

$$xg(xq_{sea}) \sim x^{-\lambda} \tag{1.31}$$

where $\lambda \simeq 0.5$.

As x decreases the standard QCD predicts a very strong rise of the density of slow gluons. At very low x a serious conflict appears: the total cross section for the scattering of a virtual photon off the proton rises faster than the unitarity limit. In other words it means that gluon density seen by the photon probe gets unphysically large. If the density of gluons within the proton becomes too large they can no longer be treated as free partons. This is an indication that the standard QCD description is not valid at $x \to 0$! Here one expects that transition from the region of perturbative QCD to the Regge limit of DIS cross sections takes place [24]. In this new regime the evolution equations must go beyond $LL(Q^2)$ perturbation approximations and reach the new regime ($\frac{s}{Q^2} \approx \frac{1}{x} \to \infty$) at fixed Q^2. Nevertheless if $Q^2 > Q_0^2$ this new regime may be studied in the framework of the perturbative QCD.

According to the proposed scenario annihilation and recombination of parton pairs are responsible for the damping of the singular growth predicted by the standard QCD. Gribov, Levin and Ryskin have tried to add a negative nonlinear term to the GLAP equation [24], leading to the GLR equation, in order to treat this effect of "screening" or "shadowing" also theoreticaly. At this point one should stress however that the nonlinear GLR equation is derived from the study of a set of Feynman diagrams and that there is no firm theoretical basis to use it in the nonperturbative region. The GLR equation can be used for the first estimate of the boundary line between the LLA and this new perturbative QCD regions (Fig. 1.4). According to this estimation we should already at HERA reach this new region. One hopes that signs of the new physics could be unveiled [26].

For low $Q^2 \approx O(1)\ GeV^2$ in the nonperturbative region, the Regge theory is used to describe the known phenomena. The input gluon distributions [2] in the structure function analysis traditionally derived from the naive Regge parton model have the following form

$$xg \sim x^{1-\alpha_P(0)} \sim constant \tag{1.32}$$

with the Pomeron intercept $\alpha_P(0) \simeq 1$.

Form (1.32) is unstable with the evolution in Q^2 (with increasing Q^2 it develops spikes at small x) and if one puts (1.23) for rather large $Q^2 \simeq 4 - 10\ GeV^2$ then with decreasing Q^2 the structure function soon becomes negative at small x. If verified experimentally, behaviour (1.31) would be a manifestation of the so-called "Lipatov" [24] or "hard" QCD pomeron with $\alpha_p - 1 = \lambda$. Unlike (1.32), behaviour (1.31) is stable with evolution in Q^2.

A short summary of the situation is shown on the Fig. 1.4. From the theoretical point of view the (Q^2, x)-plane can be divided into four regions, where different "physics" should dominate ([24],[27]):

- region A - standard DIS, perturbative QCD in $LL(Q^2)$ approximation is valid
- region B - transition region, leading log perturbative QCD still could be applied but with some restrictions or in a more sophisticated form (nonlinear term in the evolution equation)
- region C - no QCD-based theory yet, but perturbative QCD still should work
- region D - nonperturbative QCD region

[2] If one can talk about the gluon distribution in this nonperturbative region, but this language is widely used in the literature (see [25]).

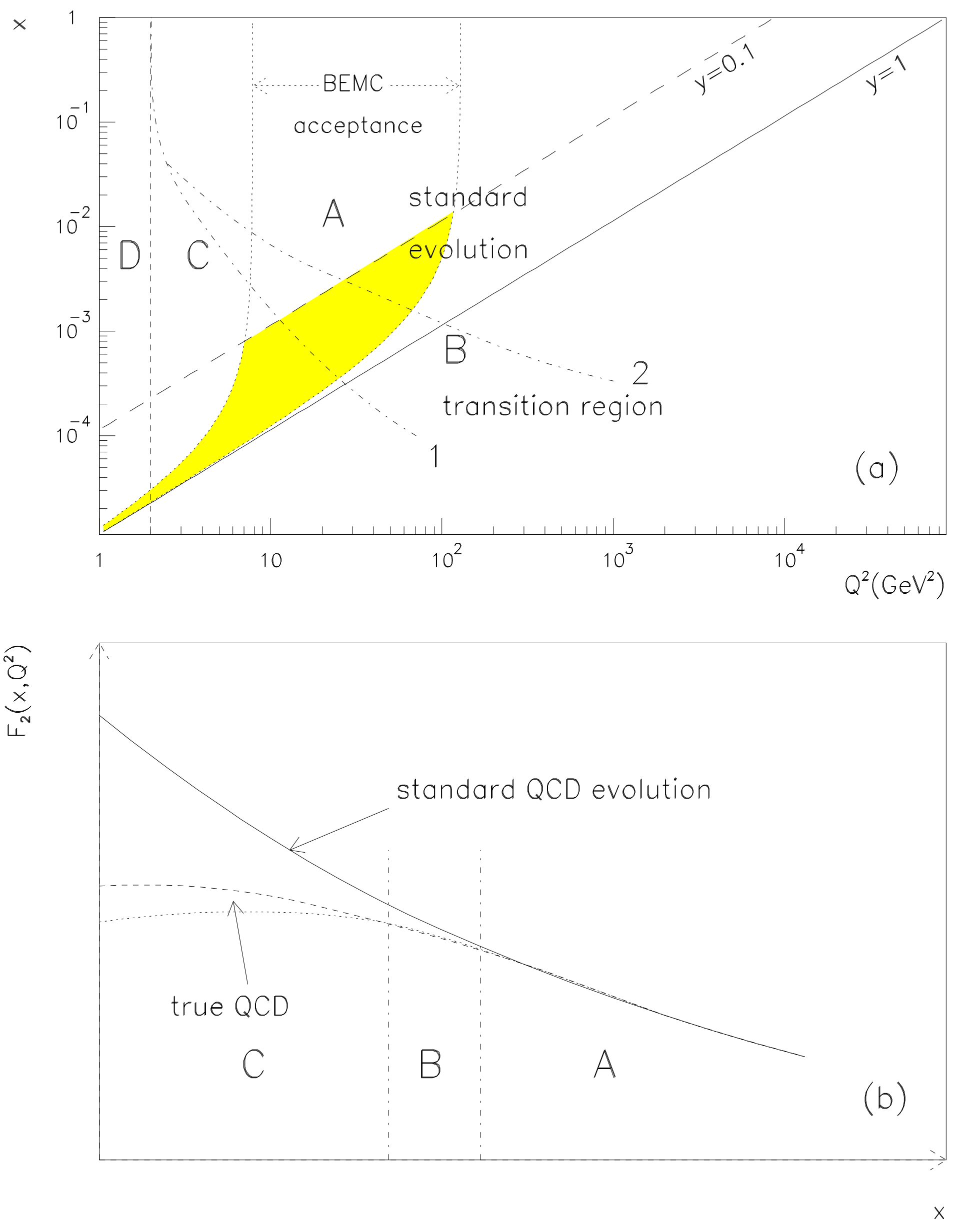

Figure 1.4: *(a) Estimation of the (Q^2, x)-plane division into LLA and nonperturbative regions according the GLR equation. The shaded area shows the region, where F_2 is measurable with the BEMC. (b) Sketch of $F_2(x, Q^2)$ evolution at fixed Q^2 according to the standard perturbative QCD. In both regions B and C the structure function should lie below the extrapolation, but the precise behaviour cannot be predicted at present.*

Experimental identification of a new regime There is no doubt that the measurements at HERA will eliminate a lot of at present available F_2 parametrizations. However an unambiguous physical interpretation of these results will be probably impossible from the F_2 measurement alone [27]. A major problem in unambiguous identification of a new regime from the $F_2(x, Q^2)$ measurements at small x alone lies in the fact that our knowledge of the nonperturbative regime is very poor and therefore:

- predictions are simply phenomenological extrapolations
- they depend on:
  - a set of "starting" distributions, $f_a(x, Q^2)$, as a function of x at some $Q^2 = Q_0^2$.
  - the presence and size of the screening corrections

As a result, we cannot be certain whether an observed steep behaviour at $x \sim 10^{-3}$ is a manifestation of the Lipatov perturbative effects or if it is due to the Q^2 evolution of the nonperturbative input x distribution. On the other hand it will be difficult to decide if the saturation of the structure function is due to the strong screening effect or to the initial flat gluon behaviour at $Q^2 = Q_0^2$.

Several alternative, dedicated measurements have been proposed to search for the unambiguous identification of the regime dominating the studied process as e.g. hot spots measurements [26], heavy photon dissociation [29], rapidity correlations between hadrons produced in DIS [30] or diffractive ep scattering [31].

1.6 Beyond DIS

HERA physics is of course not limited to the DIS. Although the aim of this thesis is to study the NC DIS, we want at least to mention some of the exciting topics accessible already with a rather limited statistics, as e.g.:

Photoproduction The largest event rate at HERA is expected from the collisions of almost real photons ($Q^2 \to 0\, GeV^2$) with protons. The study of hard scattering reactions in photoproduction is of great theoretical and experimental interest. These γp processes could reveal the anticipated internal structure of the photons. Total photoproduction cross section measurement is at HERA accessible in a range from about 100 to 250 GeV γp c.m.s. energy , i.e. extending the measured domain by more than one order of magnitude [32].

Current extrapolations of the total cross sections towards HERA energies differ substantially, therefore these values are awaited with great interest [32]. First measurements [34] are in good agreement with the Regge motivated parametrizations and seem to disfavour extreme 'minijet' models.

Hadronic final states DIS at HERA is a more complicated process than e^+e^- annihilation, but not so "messy" as at hadron colliders. Hadronic final states in leptoproduction have been studied experimentally up to invariant mass W$\simeq$ 25 GeV only. Processes with very high $Q^2 \to 10^4\ GeV^2$ accessible at HERA provide a large phase space for gluon radiation. This means appearance of multijet final states and the strong coupling constant from relative rates of these multijets events will be measurable. However this advantage is partially reduced by the big boost of the center of mass into the proton direction. This has consequences for the precise measurement of the hadronic jets in the very forward region. Among phenomena related to the QCD accessible at HERA one can mention e.g.: initial QCD radiation, hard parton emission, non-perturbative hadronization and confinement etc.

Beyond the Standard Model The large $\sqrt{s}$ energies and large momentum transfer reachable at HERA give the possibilities of observing new particles and interactions, and smaller scale structures which would provide signals for physics beyond the Standard Model.

In particular s-channel resonances in the electron-quark system, such as leptoquarks, predicted in a number of different theoretical scenarios (composite models, GUT theories), are candidates particulary suited for HERA. Since the present experimental limits are accessible at HERA, HERA has the potential for leptoquark or leptogluon discovery or at least for a significant improvement of the present experimental bounds [33]. First results from H1 point to an experimental limit of $145 - 192\,GeV$ for leptoquarks from the fusion of an electron and quark, resp. to the mass limit of $98 - 121\,GeV$ for leptoquarks formed with an antiquark. Up to now no evidence for leptogluons was found [38]. Among other processes it is also worthwile to mention e.g. [39]:

- single production of new fermions (excited leptons)
- pair production of new particles (slepton, squark)
- the study of effects from new *virtual* particle exchanges (new gauge bosons)

Chapter 2

H1 Detector

2.1 Introduction

The event topology of HERA collisions requires an asymmetric detector design since the center of mass of the collision is strongly boosted along the proton direction and consequently high particle densities and high energies are expected in the forward region.

Head on collisions of electron and proton bunches occur in the interaction region extending to $\pm 50\,cm$ along the beam axis, with respect to the nominal interaction point ($z = 0\,cm$). This *z-vertex spread* of the position of the interaction point position is due to the fact that the proton bunches are long ($50 - 200\,cm$). [1]

The innermost part of the H1 detector Fig. 2.1 is equipped with a central (2) and forward tracking (3) system. A liquid argon calorimeter consisting of an electromagnetic (4) and a hadronic (5) section surrounds the tracking system and ensures good hermeticity in the central and forward region. The backward region (see Fig. 2.3) is closed by the backward proportional chamber (BPC), the backward electromagnetic calorimeter (BEMC) (12) and the two scintillator walls (time of flight detectors - TOF). The very forward direction around the beam pipe is closed by the plug calorimeter (13).

A superconducting coil (6) with a diameter of $6\,m$ provides a magnetic field of 1.2 Tesla. This field is compensated by another superconducting coil (7) in order not to influence the HERA machine.

The magnetic flux is returned by the iron yoke (10). This yoke is interleaved with limited streamer tubes to measure the hadronic energy leakage. Muons are identified and measured by muon chambers (9) inside and outside the iron. Measurement of muon tracks in the forward region is done in the toroid (11) equipped with drift chambers.

The H1 detector is completed with the small angle electron and photon detectors placed at 33.4 and 102.9 m respectively from the nominal interaction point in the HERA tunnel, downstream of the electron beam.

In the next section we discuss the major components in more details.

2.2 Calorimetry

The H1-calorimetry is based on a large liquid argon (LAr) calorimeter, backed up by an iron tail catcher and closed by a warm backward electromagnetic calorimeter (BEMC) and a forward plug calorimeter. Electron and photon crystal detectors in the HERA tunnel are completing the H1 calorimeter system.

Basic parameters of the H1 calorimeters are summarized in the tables 2.1 and 2.2 [41].

[1] Length of the electron bunches is $\sim 1\,cm$.

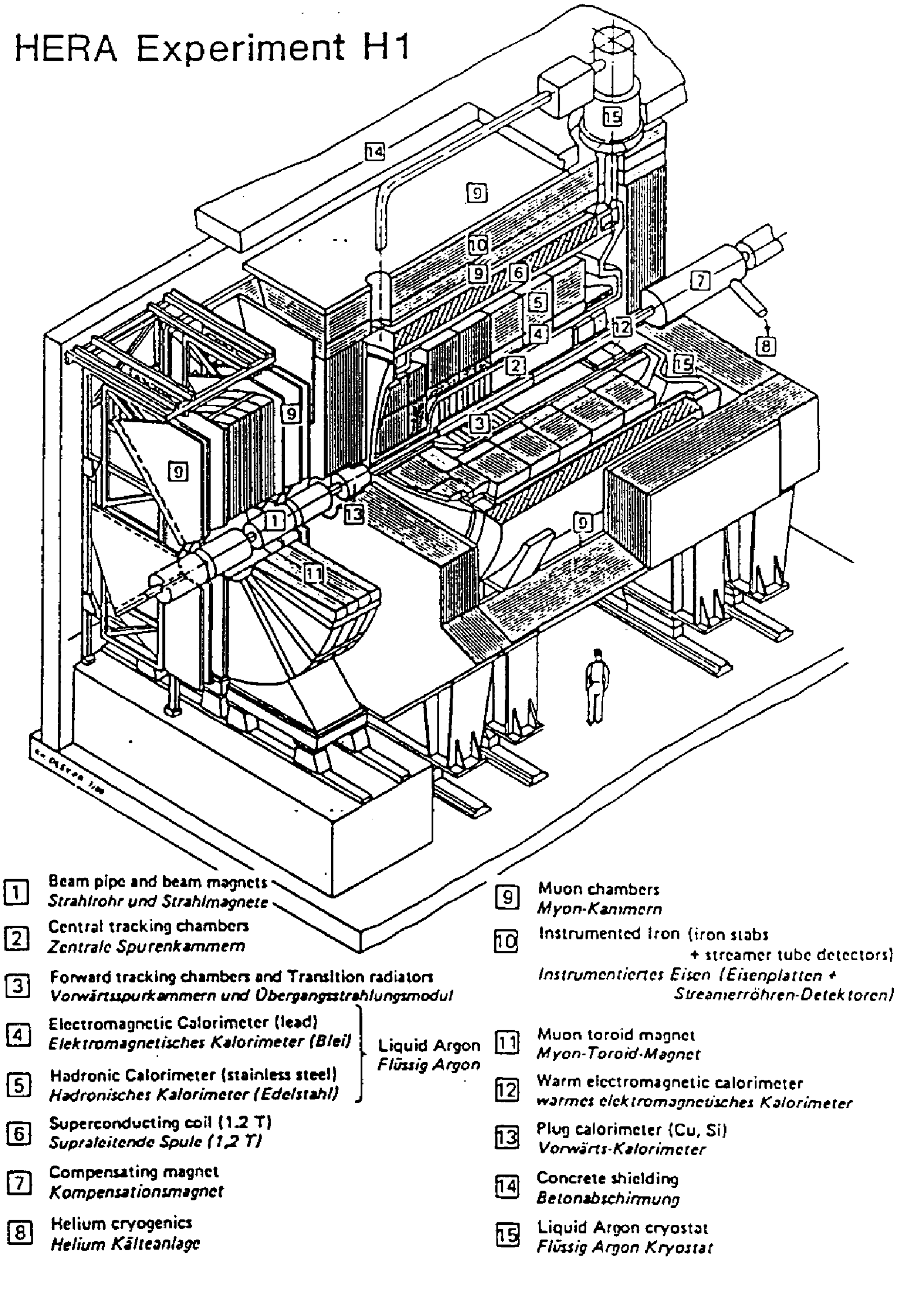

Figure 2.1: *H1 - detector at HERA*

Detector	Depth X_0	Depth λ	Transversal granularity $[cm]^2$	# of channels
LAr em	30-20	1	10-100	30784
LAr had	-	6-4	50-2000	13568
BEMC	22	1	250	88
Plug	-	4.3 (6.7)	25	336
Tail catcher	-	4.5	2500	4000
e-Tagger	21	-	5	49
γ-detector	21	-	4	25

Table 2.1: *Basic parameters of H1 calorimeters*

Detector	Calibration $\Delta E/E[\%]$	A $[\% GeV^{1/2}]$	B $[GeV]$	C $[\%]$
LAr em	± 1	$11.2 \pm .05$	$.152 \pm .004$	$.64 \pm .07$
LAr had	± 2	$46.1 \pm .7$	$.73 \pm .03$	$2.6 \pm .2$
BEMC	$< \pm 3$	10.0	-	-
Plug	-	≈ 110	-	-
Tail catcher	-	100	-	-
e-Tagger	$< \pm 1$	10	-	1.0

Table 2.2: *Energy calibration and resolution:* $\sigma/E = \sqrt{A^2/E + B^2/E^2 + C}$

2.2.1 Liquid Argon Calorimeter

The choice of the LAr for the main calorimeter was motivated by the requirements of [3]:

- longterm stability of response ($\leq 1\%$ and $\leq 2\%$ for electromagnetic resp. hadronic part) and easy calibration
- homogeneity of response
- e/π rejection $\leq 10^{-3}$ (requiring fine longitudinal segmentation)
- good angular resolution for jet directions measurements mainly in the forward region (requiring fine transversal granularity)
- energy resolution of electromagnetic part $\sigma/E \approx 10\%/\sqrt{E}$
- energy resolution of hadronic part $\sigma/E \approx 50\%/\sqrt{E}$

The design optimizes calorimeter homogeneity in order to reduce the effects from cracks and support structures (dead material). This is achieved by minimalized cracks between electromagnetic parts, and the cracks between hadronic sections have non-projective geometry. The LAr calorimeter consists of 8 independent modules (wheels) assembled along

the beamline [3]. Each of these wheels has 8 electromagnetic and 8 hadronic stacks. The only exception is the backward barrel electromagnetic (BBE) part, which has no hadronic part. The sampling structure in the electromagnetic part is built from 2.4 mm thick Pb absorber plates and 2.35 mm LAr gaps as active medium. The signal is readout by one plane of pad boards per gap.
The basic structure of the hadronic part consist of a 16 mm thick stainless steel absorber and a double gap of $2 \times 2.4\,mm$ LAr from both sides of the absorber containing a double sided pad read out board [40].

Total depths of $20 - 30\,X_0$ and $4.5 - 8\,\lambda_0$ are designed to ensure full absorption of the electromagnetic and hadronic showers with minimal leakage into the tail catcher calorimeter.
The hadronic calorimeter is not compensating, i.e. the e/h ratio response is not one, therefore a software weighting procedure is used [44]. The weighting can be used because of the fine granularity in both longitudinal and lateral directions.

2.2.2 BEMC

The BEMC is a warm sampling calorimeter in the backward region of the H1 detector ($156° < \theta < 174°$) (Fig. 2.3) which is not covered by the main liquid argon calorimeter (for more details see [47]). The BEMC is exposed to the magnetic field of 1.2 T of the H1 detector and its primary task is to measure energies of electrons scattered under small angles (in H1 convention $\theta > 156°$) from the deep inelastic processes (see Fig. 1.2).

The sampling structure is built from 2.5 mm Pb and 4 mm SCSN38 scintillator plates. While the total depth of the calorimeter in units of radiation length is $22.5\,X_0$, the corresponding nuclear interaction length is only $\approx 1\,\lambda_0$. This means that the BEMC is an electromagnetic calorimeter without containment for hadrons. The sampling structures are assembled in 88 stainless steel boxes (stacks) (Fig. 2.2). Most of them (56) have a regular rectangular shape $15.9 \times 15.9\,cm^2$. The stacks at the edge are completing the cylindrical shape of the BEMC and therefore are of a smaller size and of a irregular shapes (big and small trapezoids and triangles).

The light signal from the scintillator layers is collected and guided to the Hamamatsu S2575 silicon photodiodes by Y7 wavelength shifters (WLS).

There are 2 basic types for the geometrical arrangement of WLS - WLS covering the whole length and WLS which cover only the last third of the stack length. The first ones are called "electromagnetic" (EM) and the second ones "hadronic" (HAD) or backward channels. All stacks have 4 EM channels with the exception of small triangles with only 3 EM channels. Each quadratic stack and each big trapezoid one has in addition 2 HAD channels. In total there are 64 stacks with "hadronic" readout.

2.2.3 Plug Calorimeter

The plug calorimeter was built with the aim to minimize the missing part of the total transverse momentum due to the hadrons from the proton fragmentation, emitted close to the beam axis. This calorimeter is however placed behind larger amounts of dead material of beam pipe, LAr cryostat and of the FTD. Therefore only a moderate energy resolution for hadronic showers is required ($\sigma/E = 100\%/\sqrt{E_h}$).

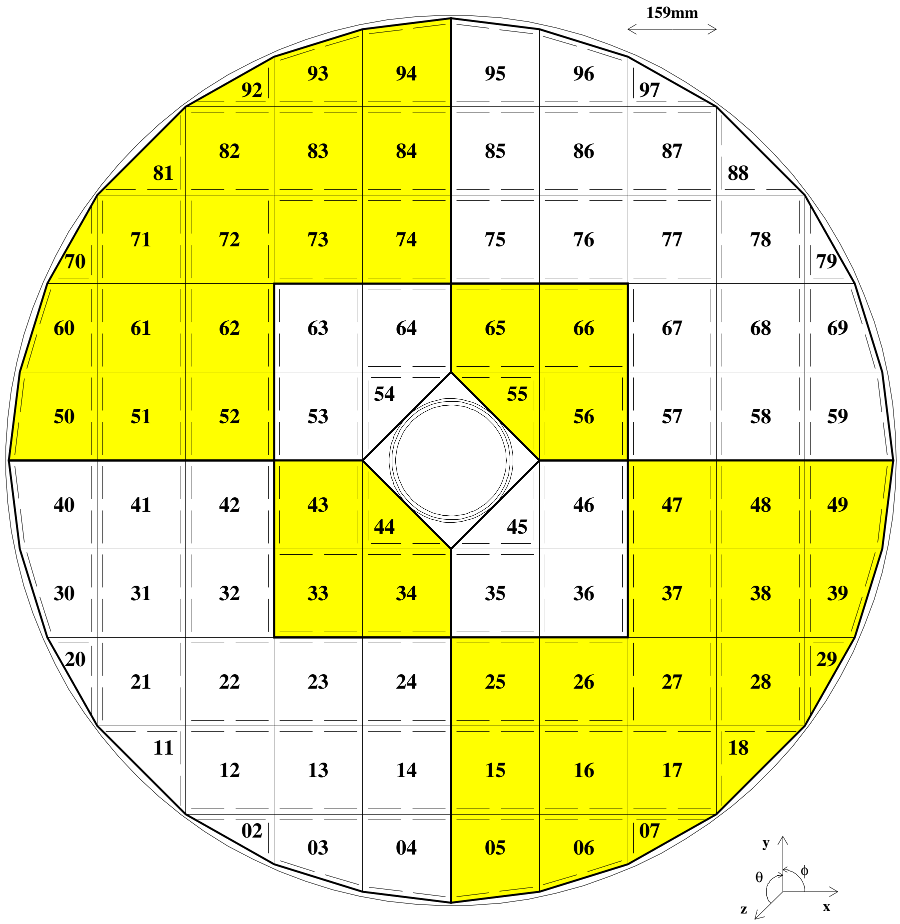

Figure 2.2: *BEMC - a frontface view from the H1 interaction point. Stack structure with the position of long wavelength shifters and numbering scheme are shown. Shaded and white areas indicate 8 trigger big towers (BT) readout by the LAr trigger.*

Due to the space limitations a very compact calorimeter design, consisting of a silicon-instrumented sandwich, was used. The plug calorimeter is built of 8 layers, each layer consisting of a 7.5 cm Cu plates and $300\,\mu m$ Si-pad detector. The total length of the instrumented part is 65 cm which corresponds to $4.3\,\lambda$. The lateral size of the basic detector cell is $5 \times 5\,cm^2$ and the radial acceptance of the plug is $6\,cm \leq r \leq 25\,cm$ or in angular units $12.5\,mrad \leq \theta \leq 60\,mrad$.

2.2.4 Tail catcher calorimeter (TC)

The hadronic energy leaking out of the main calorimeters is measured by a limited streamer tube (LST) detector [45]. The basic elements of the LST chambers are 8-fold profiles with a cell size of $9 \times 9\,mm^2$. Signals are readout from wires and strips simultaneously. A nonflammable gas mixture of CO_2, Isobutane and Argon is used $(88.5\%, 9.5\%, 2.5\%)$ instead of standard Argon-Isobutane mixture. For the detector installation the slits in the iron yoke of the main solenoid magnet are used (instrumented iron). The LAr calorimeter is thus backed by another $4.5\,\lambda$ of the tail catcher. The requirements for the hadronic energy resolution measurement are very moderate ($\sigma/\sqrt{E_h} \approx 100\%$). The tail catcher should detect only a small fraction of the jet energies. In more than 95% of the events the energy leakage into the tail catcher is less than 20% [3].

For the calorimetric part of the LST system (11 layers) the analogue signals from the pads are summed into towers and are read out through the LAr DAQ chain.

2.2.5 Luminosity Monitor and Electron Tagger

The small angle electron and photon shower counter hodoscopes located at respectively 33.4 and 102.9 m downstream of the interaction point have three separate tasks:

- luminosity measurement of the e^-p collisions
- identification and measurement of photoproduction processes
- tagging of radiative events

Both detectors, also called *luminosity detectors*, are built from matrices of KRS-15 crystals ($78\%\,TlCl$, $22\%\,TlBr$). The electron tagger (ET), with angular acceptance $0 - 5.0\,mrad$, is built from a matrix of 7×7 and the photon detector (PD) consists of a matrix of only 5×5 crystals (for details see table 2.1). Fine granularity and good energy resolution are vital for the electron tagging to study the photoproduction processes with almost real photons.

The luminosity system is completed with the $2\,X_0$ Pb filter (protection against synchrotron radiation) followed by the $1\,X_0$ water Cerenkov counter in front of PD.

2.3 Tracking Detectors

Due to the specific HERA kinematics the tracking detectors are divided into two main parts, central and forward.

The extended interaction region is surrounded by the Central Tracking Detectors (CTD) and the forward direction is covered by the Forward Tracking Detectors (FTD).

The tracking possibilities are completed with the backward proportional chamber (BPC) in front of the BEMC. The BPC is a module containing 4 wire planes rotated by 45° with respect to each other.

In the FTD two types of forward chamber modules (radial - and planar - drift chambers) are chosen to find tracks in the region where pattern recognition is expected to be difficult. The forward trackers are grouped into 3 identical supermodules, each one built from a planar drift chamber (FWP), a MWPC, a transition radiation volume and a radial drift chamber (FWR).
The radial chambers give a precise determination of the ϕ coordinate and space points are defined by the planars with different wire orientations.

The CTD is a system of proportional and drift chambers designed to fit the innermost cylindrical volume of the H1 detector (Fig. 2.3). Starting from the interaction point a particle is detected by the multiwire proportional chambers (MWPC), called CIP (central inner proportional chamber), followed by the central inner z-chamber (CIZ), the inner jet chamber (CJC1),the outer z-chamber (COZ), the outer MWPC (COP) and the outer jet chamber (CJC2).

Chamber	r $[cm]$	z_{min} $[cm]$	z_{max} $[cm]$	$\sigma_{r\phi}$ $[mm]$	σ_z $[mm]$	σ_r $[mm]$	$\sigma_{x,y}$ $[mm]$
CIP	15.3-17.2	-112.5	106.5	-	-	-	-
CIZ	17.4-20.0	-108	72	25	0.25	-	-
CJC1,CJC2	21.5-76.9	-112.5	107.5	0.21	23.5	-	-
COZ	46-49	-110.5	105.5	58	0.34	-	-
COP	50-53	-110.7	106.5	-	-	-	-
FWR	15-75	-	-	0.17	-	29.0	-
FWP	15-75	-	-	-	-	-	0.21
BPC	13.5-65	-144	-138	-	-	-	2.0

Table 2.3: *Tracking detectors sensitive regions (r,z) and resolutions ($\sigma_{r,\phi,z,x,y}$) as obtained from the first luminosity runs at HERA [41].*

The CIP and COP chambers have a good time resolution ($60\,ns$) and provide an independent determination of the bunch crossing time (t_0) for the trigger.

The task of the central drift chamber (two rings of tilted jet chambers) is a precise measurement of r, ϕ coordinates of charged tracks ($\sigma_{r\phi} = 100\,\mu m$) and a moderate z measurement from the charge division ($\sigma_z = 24\,mm$). Additionally, ionization energy measurement for charged particle identification with the design resolution $dE/dx \approx 6\,\%$ should be available [3].

Precise $z-$measurement is provided by CIZ and COZ - two sets of separated proportional $z-$chambers. The CIZ and COZ wires are stretched in a polygon installed around the CIP resp. COP. The drift direction is parallel to the beam axis and the expected $z-$resolution is $\sigma_z \leq 350\,\mu m$.

The design momentum resolution of the CJC chambers is $\sigma_{p\perp}/p_\perp^2 \simeq 3 \cdot 10^{-3}\ GeV^{-1}$ with the gas mixture $50\% Ar$, $50\% C_2H_6$. For safety reasons in the first periods of data taking the gas mixture of 89.5% Ar, 9.5% CO_2 and 1% CH_4 was used. The achieved momentum resolution was $\simeq 10^{-2}\ GeV^{-1}$, and a the dE/dx resolution amounts to about 10%.

The basic parameters of the tracking detectors are summarized in the table 2.3.

2.4 Muon Detectors

2.4.1 Instrumented iron

Muons in the central region are measured by the instrumented iron detector. *Muon chambers* are LST layers with digital read-out of the anode wires.

2.4.2 Forward Muon Spectrometer

In order to measure muon momenta in the very forward direction ($3° \leq \theta \leq 17°$) with sufficient precision a separate forward muon spectrometer (FMS) was built. The heart of the FMS is a toroid magnet with length of 1.2 m and field of 1.5 Tesla. Before and after this magnet 2 arrays, each consisting of 6 drift chambers, are installed. The drift chambers drift cells' lengths vary between 0.4 m and 2.4 m. The maximum drift distance is 6 cm and the coordinate along the sense wire is obtained from charge division measurement. Two of the double planes on either side of the toroid measure the polar angle θ and the remaining ones the azimuthal angle ϕ. The chambers are arranged in pairs with a relative shift of the sense wires by half of the drift length (3 cm). This geometrical arrangement resolves left-right ambiguities and provides a checksum (the sum of the drift times from the two offset planes) to facilitate recognition of good tracks and reject large angle punch-through. Correlated position and angle measurements for tracks at the exit of the solenoid return yoke reduce the ambiguities in linking with tracks in the central chambers. First measurements with halo muons from the proton beam showed a spatial resolution of $\sigma \leq 0.35\ mm$. The momentum resolution is expected to be $\sigma_p/p \approx 23 - 32\%$ for muons in the energy range of 25-150 GeV [41]. The resolution on the lower edge is limited by the multiple Coulomb scattering.

2.5 Scintillators

2.5.1 TOF

The time of flight (TOF) counter system placed behind the BEMC detector (Fig. 2.3) is vital for vetoing beam-gas and beam-wall background events initiated by the proton beam. The TOF itself consists of four planes of NE104 scintillator elements. Two pairs of planes create the inner and outer part of the TOF wall. The wall closer to BEMC (TOF1) is at $z = -193.7, -198.7cm$ and consists of 16 scintillator elements, each of $31.7 \times 31.7 \times 2\,cm^3$ size. The second wall further from BEMC (TOF0) located at $z = -224.3, -229.3cm$, is of bigger granularity with only 8 scintillator elements, each of $25 \times 50 \times 2\,cm^3$ size. Short maximal light paths $\approx 22.4\,cm$, resp. $28\,cm$ are an inevitable prerequisite for very good time resolution. A measured resolution of individual scintillator plates $\sigma \approx 1\,ns$ [63] ensures the TOF capability to distinguish between events originating in the interaction region and the background events originating outside, upstream of the proton beam.

2.5.2 Veto Walls

The big and small veto walls, at $z = -6.5\,m$ resp. at $z = -8.0\,m$, are built with the aim to veto particles off the proton beam axis. The big veto wall is consisting of 26 large scintillator sheets arranged in two layers covering a radius of approximately 2.5m arround the beam pipe. A square hole $60 \times 60\,cm^2$ left in the centre is covered down to a $26cm$ circle by a small veto wall placed a further $1.5\,m$ upstream [48].

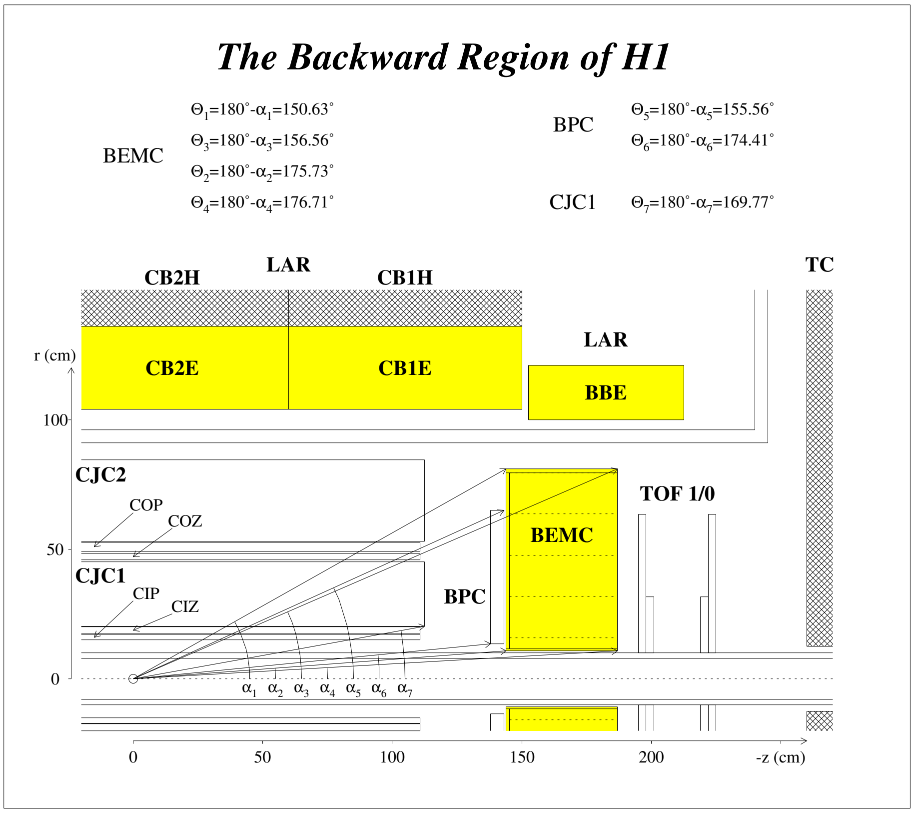

Figure 2.3: *The details of the H1 backward region with all detectors in the proper scale.*

Chapter 3

H1 Trigger

3.1 Triggering at HERA

Electrons and protons at HERA are circulating in up to 220 bunches with a beam crossing rate of 10.4 MHz, giving a clock period of 96 ns. Thus every 96 ns interactions can occur. At the design luminosity of $1.5 \cdot 10^{31}\ cm^{-2}s^{-1}$ the dominant physics process will be photoproduction at a rate of O(100) Hz. Other physics processes will contribute by a small fraction of this highest rate only. From this point of view the triggering at HERA appears as a rather trivial problem. But, as the physics cross sections are small, maximum beam currents are required. The off-momentum protons, which number is correlated with the beam current, initiate huge background rate of the order of $100\,kHz$ in the interaction region (for more details on the background rate estimation see page 41).

In fact two, at first sight contradictory tasks are required from the trigger and the data acquisition system:

- **high decision speed of the trigger** in order to minimize the dead time and to reduce the event rate down to a manageable level.
- **long signal integration time of the data acquisition system** in order to achieve the required energy and time measurement precision.

Next we discuss the solution developed within the H1-collaboration.

3.2 Frontend pipelines

The whole detector complexity, the geometrical size and differences in the basic physics detection principles of the different subdetectors are the reasons why the trigger decision cannot be made during the interval between two bunch crossings. The simple solution to buffer the frontend information and ignore the following bunch crossings untill the decision to keep the event is made is not possible. This would mean introduction of the dead time on the first trigger level (L1) and would lead to unacceptable losses of the luminosity provided by the HERA machine. The goal is to build deadtime free L1 trigger.

Therefore, the detector response for each beam crossing has to be kept in a memory until the decision is available.

To achieve this goal, the so-called frontend pipelines for the detector and trigger data flow are used. The use of a pipeline allows to postpone the trigger decision and more time is available for the detector signals processing. By analogy, one can compare a pipeline to a cable delay. Thus for each channel the time structure of the detector response can be obtained. Analog delay lines are used e.g. to store the pulseheight of the BEMC. Digital data for each beam crossing are stored sequentially and these data can be accessed at any time up to the pipeline depth (length).

The ideal pipeline length should be bigger than the longest trigger decision time, but small enough on the other hand so that it empties fast after restart. At H1 it has a length of $2.2\,\mu s$.

3.3 Multi level trigger

The trigger converts the analog information into the **trigger elements (TE)**, i.e. yes/no decisions of the individual H1 trigger components encoded in bits. Examples are encoded energy thresholds for calorimeters (E >threshold) or encoded hit patterns for multiwire proportional chambers. Each subdetector provides many trigger elements. These trigger elements are by logical functions combined into the so-called **subtriggers** and a logical *OR* from all subtriggers gives the final Level 1 **trigger decision**.

A decisive trigger parameter is speed rather than precision. It is impossible to get the final trigger decision in $2.2\,\mu s$ with a rate acceptable for the data logging on the storage media (5 Hz). Therefore together with pipelining a multi-level trigger and buffering scheme is used. For H1 the final trigger decision is supposed to be done in 4 different steps, called levels. The higher the level, the more complex and the more time-consuming is the process. The task of each level is to reduce significantly the rate of event candidates and to allow more time for a more sophisticated decision at the subsequent level.

In the first data taking period, in the year 1992, only two trigger levels were used: level 1 (L1) and level 4 (L4). Operation with only two levels was possible due to the fact that HERA machine was operated at $\sim 1\%$ of the design luminosity.

In 1992 the measured proton induced background rate was only few hundred Hz. An L1 output rate of $\sim 25\,Hz$ safely matched the L4 input limit rate of $50\,Hz$.

The final trigger decision at H1 will be done on the following trigger levels:

- **Level 1 (L1)** - An acceptable output trigger rate is 1 kHz for an expected total interaction rate of $\sim 50 - 100\,kHz$, i.e. the required reduction factor is $\sim 50 - 100$. These numbers are valid for the full HERA and H1 trigger performance.

  The dead time free first level trigger, due to $2.2\,\mu s$ decision time, must be based on the hardwired algorithms and combines only subsets of the full information available from all subdetectors. An important property is the big flexibility in combining different trigger elements from the same subdetector into complex coincidences.

  The major parameters influencing the L1 trigger efficiencies are changeable by downloading them into the electronics. The trigger performance checking and identification of defective modules or inconsistencies in the trigger logic is done by on-line monitoring.

  The L1 trigger is a rather complicated, distributed system with many additional signal delays. Precise synchronisation of all its elements is a vital task for the correct performance of L1.

  One has to ensure that all individual trigger elements are providing their decisions in a well defined time, i.e. they have to be synchronized with the HERA clock. Of course different trigger components have different decision speed. All fast trigger elements have to be delayed to wait for the slower ones. Correct timing adjustment is needed to synchronize all trigger elements. The beam crossing information provided by the subdetectors with very good time resolution, so called t_0, is treated as an independent trigger element and is needed for the proper calorimetric energy measurement, drift time measurement and for all other pipelined systems.

When analysing the L1 decision process three phases can be distinguished [43]:

1. Trigger elements from different subdetectors are produced, synchronised to the HERA clock and transferred to the central trigger logic (CTL) in groups of eight signals with accompanying clock to compensate automatically for individual cable delays and to maintain the synchronisation.
2. The CTL synchronizes all 16 groups of trigger elements and forms up to 128 different subtriggers. The *OR* of all these subtriggers eventually leads to the L1 trigger decision.
3. If the level 1 loaded trigger conditions are fulfilled $2.2\,\mu s$ after the interaction time, an $L1 - Keep$ signal is produced which initiates a well defined sequence of fast hardware signals fanned out from the central trigger controller (CTC) to all subdetectors. The frontend pipeline stops and dead time starts accumulating. A L1-reject condition implies no signal and all pipelines remain active.

- **Level 2 (L2)** - hardware trigger with dead-time, starting with $L1 - Keep$. The task of L2 is to reduce the input rate of 1 kHz to about 200 Hz. L2 decision is taken at fixed time $\approx 20\,\mu s$. The trigger elements for level 2 will be based on the same information as is used on the L1, but now more time is available to combine trigger bits from different detector parts. So called topological L2 trigger will require special hardware units utilizing characteristical topology of different physics event classes.

- **Level 3 (L3)** - software trigger, starting in parallel with L2 further reduces the rate of triggered events to maximum 50 Hz. A dedicated μ-processor will compute the L3 decision in $800\,\mu s$ on the basis of the more complex matching of the information from different detector components.

- **Level 4 (L4)** - software filter. The aim of this level is further reduction of the data volume before it is sent to the final storage media at the DESY computer center. The calculations are performed by the processor farm on the full event data, asynchronously with the rest of the trigger. Therefore this level is also called L4 filter farm. The filtering analysis is based on charged track, vertex and energy cluster information. The most important filtering criterion, effective against beam gas and beam wall backgrounds, is based on the (x, y, z) vertex reconstruction. Very important is also the recognition and rejection of the so-called 1-diode events triggered by BSET (see page 97). The aim is reduction of the final data logging rate to $\sim 5Hz$.

3.4 L1-Trigger elements from specific detectors

As already mentioned, the L1 subtriggers must be based on hardwired algorithms and only relatively crude information from the subdetectors can be utilised. Nevertheless L1 comprises many trigger elements from different parts of the H1 detector, such as energy sums from the calorimeter or veto-wall and TOF bits suppressing events initiated by the off-momentum beam particles. Particulary interesting L1-trigger elements are produced by the tracking chambers. XILINX logic cells are used for fast z-vertex position reconstruction from the proportional chambers and for the fast charged tracks finding in the $r-\phi$-projection of the central drift chamber.

Generally one can say that the main DIS physics triggers are based on the calorimeter trigger information and that the tracker trigger elements are used mainly as an effective tool to recognize the background events and reject them on the L4 level.

Subdetectors providing trigger bits for L1 are shown in Fig. 3.1.

3.4.1 Calorimetry

Liquid Argon Calorimeter

The primary task of the LAr calorimeter trigger is to select the high Q^2 events, the study of these being one of the reasons for which HERA was built. The LAr trigger itself is divided into an analog and a digital part [52] and its overall decision time is $2.1\,\mu s$ [40].

The analog sum of 16 channels in the electromagnetic (EM) or of 4 in the hadronic (HAD) part forms the basic trigger unit - called *Trigger Cell* (TC). In total almost 40000 channels are read out.

Up to 4 electromagnetic and 6 hadronic TCs are summed up and shaped to form a *Trigger Tower* (TT). The TTs are approximately pointing to the interaction point and are segmented in 23 θ-bins and up to 32 ϕ-bins. In order to allow for a bunch crossing time t_0 determination the capacities of the channels summed into the same TT must fit to $\pm 5\%$ [40].

Depending on the θ-region, either 1,2, or 4 TTs are summed up to form a *Big Tower* (BT). BTs are organized also according to the principles of projective geometry, they are pointing to the vertex. There are in total 252 BTs, 240 in the LAr calorimeter itself and additional 8 BTs in BEMC, resp. 4 BTs in plug calorimeter.

In the digital part the energies of the corresponding EM and HAD sections are digitized by 8-bit 10 MHz FADCs and summed up into BT-energies after relative weighting by lookup tables. Further summing of BTs, again according to the corresponding lookup tables, results in the different energy sums. Digital part provides following trigger elements sent to the central trigger logic:

- *electron trigger*
- *transverse energy*
- *total energy*
- *missing transverse energy*
- *topological energy sums*
  Plug, Inner Forward (IF), Forward (IF+Plug),
  Central Barrel (CB), Forward Barrel (FB), Barrel (FB+CB),
  BEMC, Backward (CB+BEMC)

- *BTs* t_0
- *Big Rays* t_0 (BTs t_0 matched to the MWPC big ray)

The division into 8 topological regions is hardwired and each of these regions is subdivided into 4 ϕ-quadrants. This gives altogether 40 topological trigger sums (with 8 total energies). The total and transverse energies are added separately. Each energy is discriminated by a 2-bit table, allowing definition of 3 thresholds.

The energies of the EM and HAD parts of the individual BTs are used to build an electron trigger. Energy in the EM part has to be above a given threshold, whereas energy in the HAD must be below some threshold.

BEMC and Plug

The BEMC and plug trigger are an integral part of the L1 overall calorimeter trigger. BEMC is divided into 24 TTs and 8 BTs (Fig. 2.2) and plug is subdivided into 16 TTs and 4 BTs.

BSET

A special BEMC single electron trigger (BSET) with smaller granularity was designed and realised in order to cope with the expected high rates in the backward part of H1 (for details see page 72).

3.4.2 Tracking System

MWPC Triggers

Trigger signals from the MWPC are derived from the two double layers of CIP and COP in the central region at average radii of 16 cm and 52 cm, and three double layers of MWPC (modules) in the forward region centered at $z = 146$, 188, 231 cm [60]. The combinations of the hits in various chambers define trajectories (rays) with a precision given by the cathode pad size and the spacing between the chambers.

These rays are then used to provide two types of trigger information :

- *z-vertex trigger* - A hardwired logic finds so-called *rays* from z-coordinates of all possible hit combinations in the CIP and COP pair or in the CIP and the first forward MWPC pair. The z-coordinate of the origin of each ray enters the 16 bin histogram (5 cm/bin). Inevitably also combinations not originating from true particle tracks are entered, however these 'wrong' rays generally produce a flat z-distribution. If there is at least one entry into the histogram the $ZVTX - t_0$ trigger element is produced. So the $ZVTX - t_0$ is a rather weak condition indicating some activity in the H1 interaction region. A significant peak in the z-vertex histogram is considered as a strong signal for an event originating in the interaction region. Two different significance thresholds are used and the corresponding trigger elements are called $ZVTX - sig1$ and $ZVTX - sig2$. The final histogram building and the peak analysis is done by the programmable logic cell arrays (XILINX).

- *forward ray trigger* - The forward ray trigger identifies trajectories (roads) of charged particles coming from the interaction region ($\pm 25\,cm$). A road is a set of impacts on 3 or 4 MWPC modules in one $2\pi/16$ ϕ sector. Among the 6 or 8 chambers (2 chambers per module) only one is allowed to miss the track, which was detected by the others. An estimation of tracks multiplicity for each sector is also made. Topological pattern code gives some information on the event topology in $2\pi/8$ ϕ granularity. The 256 different patterns are grouped into 30 different classes. Patterns in each class can be derived from each other from symmetry principles. Patterns are fully programmable and e.g. two back to back roads with low multiplicity per ϕ sector can be required.

- *big rays* - a big ray corresponds to at least one ray found by the ZVTX or forward ray trigger and pointing to a calorimeter big tower.

- *BPC trigger* - if at least three out of four planes of the backward MWPC (BPC) have seen a hit, the BPC trigger element is produced.

- *CIP trigger* - if more than three sectors in the backward quarter of the CIP are active, the CIP-backward trigger element is produced. This element is used mainly as a veto for some subtriggers which are using tracking information only.

Drift chamber trigger

The information from the central jet chambers is used to find and count charged tracks [61]. The track finding logic works fully parallel in the $r - \phi$ projection of the whole chamber on the subset of 870 out of the total 2160 sense wires of the CJC1 and CJC2. The signals above the threshold from selected wires are fed into shift registers. The outputs of shift registers are compared with a large number of predefined patterns corresponding to different ϕ angles and different $p_\perp$ cuts and charge. In the trigger only 10 out of 56 layers of sensitive wires are used. These ten layers of wires are divided into two groups. Only hits in four out of five layers within one group are required to form a valid pattern, so called trigger road.

Restricting the $R - \phi$ origin of the tracks to be very close to the beam axis (distance of closest approach - DCA) is an effective tool to reduce the background and noise events rates [61].

The $DC - r\phi$ trigger logic provides the number of track candidates for positive and negative curvatures above two programmable transverse momentum thresholds and topological correlations between tracks can be programmed as well. E.g. trigger elements $DC - r\phi - thr0$ and $DC - r\phi - thr1$ are used for finding at least 1 resp. more than 1 track candidates in the interaction region.

3.4.3 Luminosity system

Three basic trigger elements are used in the central trigger logic:

- ET (electron tagger) total energy
- PD (photon detector) total energy
- VC (veto counter) signal

For luminosity measurements a stand alone system, independent from the central trigger and DAQ is needed. For this purpose the bremsstrahlung process $e^-p \rightarrow e^-\gamma p$ is used. Simultaneous measurement of γ and scattered electron requires coincidence between energies deposited in ET and PD. Cerenkov counter in front of PD can be used as a veto (VC) for events in which bremsstrahlung photons interacted in the Pb filter.

The total photoproduction cross section measurement is the second very important task of the luminosity system. A typical and clean signature for the photoproduction process (γp), i.e. the interaction of quasi-real photons $Q^2 \rightarrow 0\,GeV^2$ with protons, is the following: no activity in the PD and an energy deposit in the ET above some threshold. But the huge background from the above mentioned bremsstrahlung process (24.3 mb of accepted cross section compared to $\sim 1.4\,\mu b$ for γp [62]) and from the beam-gas background interactions makes this method only marginal and does not provide a reliable measurement of $\sigma^{tot}_{\gamma p}$ [62].

In order to measure the $\sigma^{tot}_{\gamma p}$ one has to rely on an alternative method: tagging of the scattered electron in coincidence with the trigger elements of the main H1 detector. For triggering on secondaries created at the γp vertex the tracker triggers are most effective. The electron tagger as a subtrigger requires a coincidence of the total energy of ET with a veto from the PD ($ET * \overline{PD} * \overline{VC}$).

3.4.4 Muon system

Inclusion of efficient muon triggers covering a large solid angle, substantially increases the physics potential of H1 [48]. Muon triggering and measurement is for many processes complementary to electron triggering and allows a comparison between channels involving intrinsically the same physics, but with different systematic effects. Only to name a few of the physics processes, which need a good muon trigger one can mention:

- heavy-flavour physics; accessible through the $\sim 10\%$ semi-leptonic decay fractions of charm and beauty states
- J/ψ photoproduction; accessible through the decay into $\mu^+\mu^-$
- exotic phenomena; search for excited leptons or supersymmetric particles

A second important asset is the possibility of cross-calibration of the other parts of the H1 detector. This can be done by cosmic or beam-halo muons, and muons from the physics channels.

Central muon trigger The first level muon trigger is based on the digital readout of the tail catcher calorimeter layers (*muon chambers*) [46]. Each wire from the LST system is digitized and the number of output signals is reduced by factor 16 via applying a logical OR on groups of 16 wires. These fast trigger outputs of five, from the total 12, LST chamber layers (3,4,5,8,12) are sent to the central trigger loggic.

The configuration of the trigger electronics is programmable and provides a very flexible solution to meet many different requirements. The whole LST detector is divided into 4 *sectors* (forward and backward endcap, forward and backward barrel), within each of these sectors chambers are grouped into 16 different modules. Signals from the five trigger planes are treated separately for each module in a so called *layer coincidence*. Trigger signals within the planes are OR'd and outputs from 5 planes are in the correspondig RAM combined according the required logic. Each RAM provides 8 bits for further usage and in total 64×8 signals can be combined.

Forward muon trigger

Muon track candidates are selected only if they have hits in both modules in front of or in both modules behind the toroid (pre- resp. post-toroid muons). For triggering purposes only the θ-chambers are used, the usefulness of ϕ-chambers being limited by multiple scattering. The requirement on the pointing of the track to the z-vertex efficiently reduces rate of background events [48].

3.4.5 Scintillators

Scintillator triggers are designed mainly to veto background events. Their very good time resolution of ~ 1 ns enables them to provide very important time information for the H1 trigger system and allows precise synchronisation of the triggers with respect to the beam interactions.

Veto Walls

Experience of UA1 shows that high momentum muons originating a long way upstream of the detector, so called *beam-halo*, could be misinterpreted as high Q^2 interactions and this kind of background is best vetoed by this type of detector [48]. Nevertheless, the potential of this trigger element was not fully used in the year 1992.

TOF

The veto function of the TOF is based on the time of flight difference of ~ 14 ns between the arrival of particles originating upstream and inside the interaction region.

Most of the secondary particles from the background interactions will be absorbed by the different beam line and shielding elements, but the particles concentrated in a narrow cone around the beam axis will enter the H1 detector or hit the synchrotron radiation absorber mask at around $z = -3$ m. Monte Carlo simulations showed that there is substantial yield of secondary particles of high energies, which cause big energy depositions in calorimeters and a lot of tracks in the central region [48]. A large fraction of these out of time events is vetoed by the TOF, therefore most physics L1-triggers require a veto from this detector.

Signals from particles originating in the interaction region (*interaction (IA) window* or *positive TOF*) are used as well, mainly for triggering of the so called high-y events. TOF triggers in the IA-window exploit the information from the leakage of high energy electromagnetic showers and/or from the punch-through hadrons accompanying low energy electrons.

In addition, the TOF wall also covers a small beam-halo window left in the veto wall because of the physical constraints of beam-line elements.

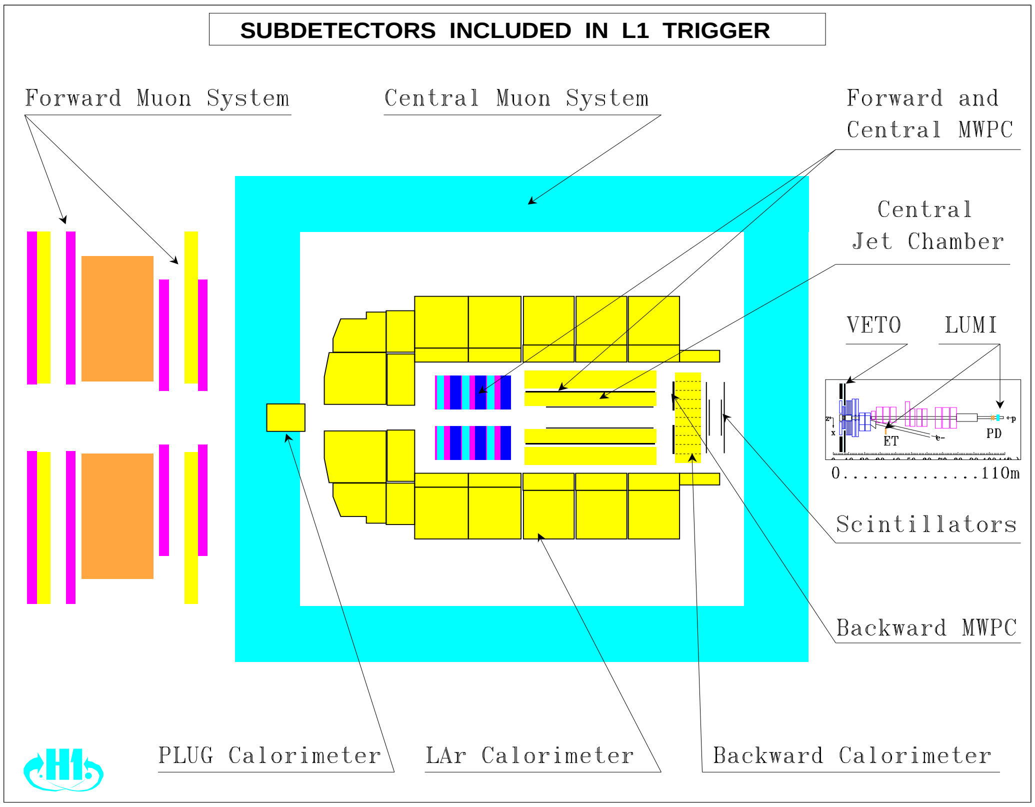

Figure 3.1: *H1 detectors in L1 trigger*

Chapter 4

Trigger for NC DIS

4.1 General requirements

Triggers are needed in order to reduce the rate of potentially interesting events to a level manageable by the data acquisition system. In the presence of a large number of different event topologies and similarities even with background events it is usually impossible to come to a required unique solution in a very short available time. At this point one has to be very cautious, because the price for the higher selectivity (lower rates) could be uncontrollable losses of certain events class leading to a bias in the trigger. A reasonable compromise between selectivity and controlled losses must be chosen.

A trigger is not necessarily associated directly with a particular physics process. Triggers are usually designed to identify and measure the physics objects or quantities which characterize the physics signal. So called *physics triggers* as electron, muon, jet or missing transverse energy E_T (neutrino) triggers have been designed. Basic requirements for the trigger system aimed for any physics class are the following:

- **high efficiency** - preferably $\geq 50\%$, computable and known to adequate precision
- **minimum bias** - the resulting trigger efficiency should not depend on the physical model
- **background rejection power (selectivity)** - fraction of triggered background events should be minimal
- **simplicity** - the trigger must be as simple as possible, in order to be well controllable and understandable
- **reliability (robustness)** - stable and reliable performance, not very sensitive to the detector performance (noise) and different background conditions (e.g. beam quality)
- **redundancy** - it is desirable to have at least two independent triggers covering the same kinematical region to cross-check their efficiency, to calculate the acceptance
- **overlapping triggers** - smooth covering of the whole kinematical region, overlapping on the boundaries to avoid discontinuities in the efficiency

4.2 NC DIS Triggers

When looking for the efficient trigger for NC DIS, it is clear that the main trigger must be an e^--trigger, based on the calorimeter information. Deposition of substantial, well localized energy in the calorimeter is the most powerful electron selector. Calorimeter triggers relying on the electromagnetic showers energy measurement have a high efficiency, they are robust, relatively simple, controlable and independent of a model assumptions.

Tracker detectors are used to trigger on the hadronic final states of the DIS. Since the processes of initial and final state QCD radiation, fragmentation and hadronization procceses at HERA energies are only extrapolated from scattering at lower energies, they are not well known and there exist a lot of different models trying to predict the event topology. Therefore trigger algorithms prepared on the basis of MC simulation are model dependent and can introduce bias. Tracker triggers will be used mainly for cross-checking the calorimeter trigger performance and as a main triggers only in the regions not accessible to calorimeter triggers. They are very effective on the L4 level, filtering out the beam-wall and beam-gas background events.

Triggers combining calorimeters and tracking detectors are used to cover some regions inaccessible by calorimeter triggers alone.

Thus we divide our triggers into three classes:

- *calorimeter triggers*
- *tracker triggers*
- *combined triggers*

When studying the kinematics of the NC DIS (Fig. 1.2). and taking into account that our main triggers should be calorimeters, we come to the natural division of the NC DIS events into two classes:

1. **low Q^2 events** - $Q^2 \leq 100 GeV^2$, scattered electron is in the BEMC
2. **high Q^2 events** - $Q^2 \geq 100 GeV^2$, scattered electron is in the liquid argon calorimeter

Of course, there is no sharp boundary line at $Q^2 = 100\, GeV^2$. The existing overlap in the geometrical acceptance between the BBE part of the LAr and the BEMC and the smearing of the $z-$vertex position are the reasons for the kinematical overlap in Q^2 between 80 and $150\, GeV^2$.

In our further studies we will concentrate mainly on the low Q^2 physics with the aim to find efficient trigger algorithm covering this very promising kinematical region, which is going to be the so called *first days physics*.

4.3 Background to the NC DIS Events

4.3.1 Physics Background

The main physics background for the NC DIS at low Q^2 is coming from the photoproduction process. These events have usually low energy activity in the H1 detector and in addition resolved photon interactions tend to produce hadrons in the backward region. The potential of the L1 trigger to separate photoproduction from NC DIS process is in this region very limited. For a large fraction of these events the electron is detected in the electron tagger. But still high rates of non tagged γp events produce signals in the BEMC. Hadrons and photons could mimic a NC DIS electron. Especially the region of low cluster energies ($< 10\,GeV$) close to the beam pipe is expected to be strongly contaminated by these events.

4.3.2 Machine Background

The biggest source of background at HERA comes from the electron synchrotron radiation. This radiation is predominantly soft and close to the beam axis thus should cause no trigger problems [48]. The main problem for the first level (L1) trigger at HERA is the rate of background events originating from the proton beam. An example of a typical HERA background event is shown in the Fig. 4.1. According to the production mechanism we distinguish two dominant sources induced by the proton beam [3]:

- **Beam-gas** interactions of primary protons with the residual gas in the beam pipe
- **Beam-wall** interactions of the off-momentum protons from the beam with the beam pipe wall producing high energy hadronic showers

Due to the fact that these are both strong processes and the e^-p collision is an electroweak process, the background rates are much higher than the physics ones.

Rates prediction

The rates for the machine background events are difficult to estimate reliably, they are much more uncertain than the physics rates. Nevertheless the following estimates were made.

- **Beam-gas** interaction rate strongly depends on the assumptions about the beam pipe vacuum quality, i.e. about the residual gas density and about the composition of this gas. For the HERA vacuum the values ranging from 1×10^{-9} to 3×10^{-9} $Torr$ were used.
  Concerning the rest gas composition, e.g. the PETRA as well as the SIN vacuum group claim that the rest gas is mostly H_2O. At HERA the rest gas composition [49] is expected to be from 50% H_2 and a heavier components $\sim 50\%\,(H, C, O)$ or air might be present in the warm HERA sections. Second important factor influencing the final rate estimate is the number of protons in the ring or the proton beam current. Here the designed value of 2×10^{13} protons in the ring is used (this corresponds to $\sim 160\ mA$).

  Another factor increasing the beam-gas events rates is the length of the collider straight section before the interaction point. HERA experimental areas are sensitive from $\sim 100\ m$ upstream the proton beam.

  The total rate of the beam-gas interactions W can be calculated from the following equation [50]:
  $$W = n_p \cdot \nu_p \cdot \sigma \cdot A^{0.7} \cdot n_{gas}$$
  where:

  - n_p - proton beam density $(2 \cdot 10^{13}/6.3 \cdot 10^5[cm^{-1}])$
  - ν_p - protons relative velocity $(3 \cdot 10^{10}[cm \cdot sec^{-1}])$
  - $\sigma \cdot A^{0.7}$ - p-gas cross section $(35 \cdot 10^{-27} \cdot A^{0.7}[cm^2])$
  - A - gas atomic weight
  - n_{gas} - number of gas atoms at $10^{-9} torr (7.2 \cdot 10^{13}/A)$

  From these assumptions the obtained rate of the beam-gas events is $\sim 3kHz/m$ and rate of events producing at least one t_0 in any of H1 subtriggers is predicted to be $\sim 35\ kHz$ [79].

- **Beam-wall** interaction rate is determined by the lifetime of the proton beam and of course by the number of protons in the ring. Proton beam losses occur along the whole HERA ring but the main losses are expected at collimators in the straight section West of the HERA ring. They absorb most of the off-momentum protons. However a small fraction of these protons survive (~ 1 %) [3] and impact at the QS quadrupole magnet ($z \simeq -40\ m$). Decisive for the rates observed in the H1 detector are therefore the proton beam losses at this QS quadrupole magnet. Assuming a proton beam lifetime of 20 hours, an average proton loss rate $5.0 \cdot 10^5 s^{-1}$ at this critical place is expected. So the final beam-wall interaction rate in the experimental areas is expected to be $\sim 70\ kHz$ [79]. It is only by factor ~ 2 higher, when compared to the beam-gas events (BGE), but additionaly the beam-wall events (BWE) energy spectrum is harder, more aggressive than the beam-gas background.

Rates first measurements

Experimentally it is not easy to identify unambiguously and separate beam-wall and beam-gas background events. Therefore only the total measured rate is given. From the first comparisons, with the proper scaling to the delivered beam currents, it seems that the predictions were a little bit too pessimistic. The observed rate, which is strongly correlated with the beam conditions and can change from run to run, was by factor $\sim 2.5 - 5$ smaller as expected [79]. Nevertheless, taking into account all uncertainties connected with the estimation of these quantities, this result can be considered as a good agreement. Simulations of the BWE and BGE (see page 45) based on the above mentioned assumptions proved to be very useful and inevitable tool in the process of preparation of suitable trigger algorithms for specific physics processes.

Synchrotron radiation as a source of high background rates was originally considered as unimportant. But first data analysis indicate that direct hits of BEMC photodiodes creates a lot of fake cluster triggers. For more details see page 99.

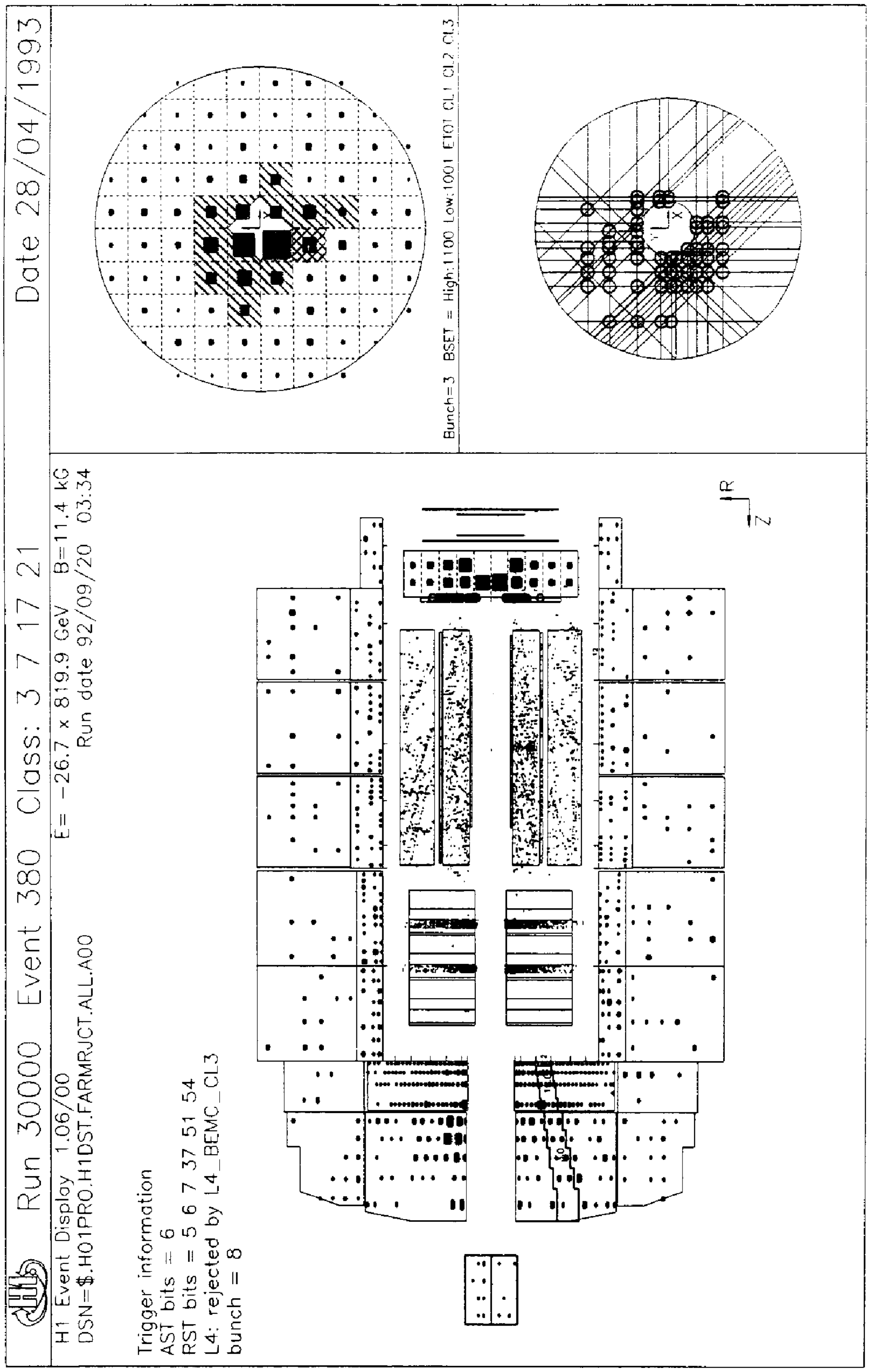

Figure 4.1: *Typical HERA background event in the H1 detector with large energy deposit in the BEMC stacks concentrated around the beam pipe and many BPC hits.*